MNRAS 000, 1–17 (2026) Preprint 22 July 2026 Compiled using MNRAS LATEX style file v3.3

An (in)complete NIRSpec census of Balmer absorption in Type 1 AGN – radiation-driven outflows in little red dots, quasars and variable stars

Ignas Juodžbalis,[1,2★] Xihan Ji,[1,2] Francesco D'Eugenio,[1,2] Jan Scholtz,[1,2] Roberto Maiolino,[1,2,3] Amanda Stoffers,[1,2] Alessandro Marconi,[4,5] Elena Bertola[5], Andrew J. Bunker,[6] Stefano Carniani,[7] Giovanni Cresci,[5] Emma Curtis-Lake,[8] Zheng Ma,[9] Cosimo Marconcini,[4,5] Eleonora Parlanti,[7] Pierluigi Rinaldi,[10] Brant Robertson,[11] Hannah Übler,[12] Giacomo Venturi,[5] Junyu Zhang[9]
[1]Kavli Institute for Cosmology, University of Cambridge, Madingley Road, Cambridge, CB3 0HA, UK
[2]Cavendish Laboratory, University of Cambridge, 19 JJ Thomson Avenue, Cambridge, CB3 0HE, UK
[3] Department of Physics and Astronomy, University College London, Gower Street, London WC1E 6BT, UK
[4] Dipartimento di Fisica e Astronomia, Università degli Studi di Firenze, Via G. Sansone 1,I-50019, Sesto Fiorentino, Firenze, Italy
[5] INAF - Osservatorio Astrofisico di Arcetri, Largo E. Fermi 5, I-50125, Firenze, Italy
[6] Department of Physics, University of Oxford, Denys Wilkinson Building, Keble Road, Oxford OX1 3RH, UK
[7] Scuola Normale Superiore, Piazza dei Cavalieri 7, I-56126 Pisa, Italy
[8] Centre for Astrophysics Research, Department of Physics, Astronomy and Mathematics, University of Hertfordshire, Hatfield AL10 9AB, UK
[9] Steward Observatory, University of Arizona, 933 N. Cherry Avenue, Tucson, AZ 85721, USA
[10] Space Telescope Science Institute, 3700 San Martin Drive, Baltimore, Maryland 21218, USA
[11] Department of Astronomy and Astrophysics University of California, Santa Cruz, 1156 High Street, Santa Cruz CA 96054, USA
[12] Max-Planck-Institut für extraterrestrische Physik (MPE), Gießenbachstraße 1, 85748 Garching, Germany

Accepted XXX. Received YYY; in original form ZZZ

ABSTRACT

A notable achievement of the first generation of JWST surveys was the discovery of an abundance of faint high-redshift ($z > 4$) broad-line active galactic nuclei (AGN) in the $L_{\rm bol} < 10^{45}$ erg s^{-1} regime, previously only accessible at $z < 1$. The high prevalence of absorption features in their broad hydrogen lines is one of the peculiarities of a significant fraction of this new population. In this paper, we conduct a broad census of Balmer absorption in a sample of 47 Type-1 AGN spanning $2 < z < 7$. Accounting for incompleteness of JWST spectroscopic data, we estimate that 44^{+21}_{-6} % of Little Red Dots (LRDs) have absorption in Hα while the incidence rate is < 25 % (at 2σ) in Little Blue Dots (LBDs). Additionally, R1000 JWST/NIRSpec data is strongly resolution limited, implying an inability to disentangle Doppler broadening in the absorption from optical depth effects. This is alleviated with R2700 observations, although some degeneracies remain. We find a significant correlation between the velocity of the Balmer absorption and the [OIII]5007 narrow line luminosity, suggesting a common driving mechanism. We do not find any other significant correlations (and do not confirm previously claimed correlations) between Balmer absorption and other spectral properties of LRDs (except for the expected correlation between Hα and Hβ absorption velocities). Comparing LRDs, quasars and stellar Hα absorbers, we establish that absorption in both LRDs and broad absorption line quasars is consistent with radiatively driven outflows, echoing the physics of variable stars yet occurring at vastly different scales.

Key words: galaxies: active – galaxies: Seyfert – ISM: jets and outflows

1 INTRODUCTION

The discovery of a large population of faint active galactic nuclei (AGN) at high redshifts (e.g. Kocevski et al. 2023; Matthee et al. 2024; Maiolino et al. 2024a; Harikane et al. 2023) was one of the first accomplishments of early James Webb Space Telescope (JWST) surveys. However, this faint population quickly revealed itself to be peculiar relative to their more luminous counterparts. Despite showing clear broad hydrogen lines contributing well over 60% of the total Hα flux (Matthee et al. 2024; Juodžbalis et al. 2026a; D'Eugenio et al. 2025), these sources appear to be nearly universally X-ray weak with non detections even in the deepest Chandra fields (Ananna et al. 2024; Maiolino et al. 2025; Sacchi & Bogdán 2025; Yue et al. 2024). In addition, a substantial subset of these AGN exhibit 'v' shaped continua – with blue slopes in the UV contrasting with the red optical emission with the turnover always occurring around the Balmer break (Setton et al. 2025). Dubbed 'Little Red Dots' (LRDs), these objects became a source of significant debate with early models proposing a mix of old stellar populations and different dust attenuation to explain the unusual continuum shapes (Kocevski et al. 2023; Casey et al. 2024; Labbé et al. 2024). However, these initial models struggled with the inferred compact sizes and large masses of LRDs, which implied extreme stellar densities if the 'v' shaped continua were interpreted as stellar Balmer breaks. This was partially resolved by Inayoshi &

★ E-mail: ij284@cam.ac.uk

Maiolino (2024) demonstrating that any obscuring hydrogen gas at sufficiently high ($n_H \sim 10^9$ cm^{-3}) densities could produce a Balmer break in the transmitted continuum, while attenuating the X-rays produced by the central engine. This framework was quickly demonstrated to be successful at modeling LRD spectra without invoking massive stellar populations (Ji et al. 2025a). This family of models attempt to reproduce LRD emission through invoking dense gas shells blanketing the central engine and resembling stellar atmospheres, dubbed the black hole star (BH*; Naidu et al. 2025; de Graaff et al. 2025b). While successful in reproducing LRD continuum shapes, these models raised their own tensions – the implied extreme column densities ($N_H \approx 10^{25}$ cm^{-2}) suggest that the observed broad-lines widths may be the result of electron scattering effects rather than virial broadening, although this is in tension with the claim of a black-body-like emitting pseudo-atmosphere, unless this is clumpy or has openings (Ji et al. 2026; Tang et al. 2026; Geris et al. 2026; Sok et al. 2026). The finding that a significant fraction of LRDs (about 50%) have exponential Hα profiles (Rusakov et al. 2025; Scholtz et al. 2026b) has been used to suggest that black hole (BH) masses may be overestimated by an order of magnitude if standard virial calibrations are used (Rusakov et al. 2025). However, recent findings that exponential line profiles can be produced by stratification in the broad line region (BLR) by Scholtz et al. (2026b); Madau et al. (2026) and a dynamical BH mass measurement of Juodžbalis et al. (2026b) contradict the idea that scattering in an optically thick medium is the main line broadening mechanism in LRDs. Nevertheless, the prevalence of Balmer absorption features in LRD spectra (Matthee et al. 2026; Juodžbalis et al. 2024a; Lin et al. 2026) clearly indicates the presence of an optically thick medium in these sources. While this dense gas has often been associated with a pseudo-stellar atmosphere embedding the growing black hole, simpler models invoking the classical equatorial dusty obscuring medium around a highly accreting black hole have also been proposed (Madau & Maiolino 2026a,b).

While X-ray attenuation in a Compton-thick medium remains an attractive explanation for the X-ray weakness of LRDs (Comastri et al. 2026), their blue counterparts – Little Blue Dots (LBDs), defined in Brazzini et al. (2026); Geris et al. (2026) – resemble regular Type 1 AGN in their UV–optical spectra yet share the extreme X-ray weakness of LRDs while appearing to lack the deep Balmer absorption lines of the latter. In addition, while the incidence rate of Hα absorption in LRDs is generally high, with recent estimates placing it as high as 60% (Matthee et al. 2026; Lin et al. 2026), deriving a precise occurrence rate is non-trivial due to inherent incompleteness in JWST spectroscopic data, most of which is taken at R1000 or even lower resolution which can miss rest-frame absorbers (D'Eugenio et al. 2026). In this paper we construct a sample of Hα absorbers from archival JWST data and obtain a completeness corrected estimate of the absorber incidence rate across both LRD and LBD populations. We then move on to investigating the ability of JWST data to recover the properties of the detectable Hα absorption features and review the demographics of our absorber sample, discussing their implications for the BH* and alternative models of LRDs. Lastly, we investigate the apparent similarities between LRDs and other broad-line emitters with Balmer absorption: FeLoBALs - a subset of broad absorption line (BAL) quasars (QSOs) (Aoki et al. 2006; Choi et al. 2022; Leighly et al. 2025) and emission-line stars (Leitherer & Zickgraf 1987; van Genderen 2001).

The paper is organized as follows – in Section 2 we provide an overview of the data used as well as our absorber selection criteria, BLR fitting and LRD - LBD classification. Section 3 presents our completeness simulations and parameter recovery tests as well as the completeness corrected Hα absorption incidence rates for LRDs, LBDs and the combined AGN population. Section 4 presents an overview of the absorber demographics and their comparison to the BH* model predictions along with the observed non trivial correlations between the absorber properties. Section 5 contains the extended discussion on the similarities and differences of LRDs and FeLoBALs as well as parallels between Hα absorption in AGN and emission line stars. Lastly, Section 6 presents our conclusions and future outlook.

Throughout this work we assume a flat ΛCDM cosmology with $\Omega_m = 0.315$, $H_0 = 67.4$ km s^{-1} Mpc^{-1} (Planck Collaboration et al. 2020). All reported magnitudes are in the AB system (Oke & Gunn 1983).

2 DATA DESCRIPTION AND SAMPLE SELECTION

The data used in this study originates from three JWST NIRSpec MSA surveys - JADES (PIDs 1210, 1287, 1286, 1181 and 1180, Eisenstein et al. 2023; Bunker et al. 2023; D'Eugenio et al. 2024; Curtis-Lake et al. 2026), CEERS (PID 1345, Finkelstein et al. 2023) and RUBIES (PID 4233, de Graaff et al. 2025a) as well as the NIRSpec IFU surveys BlackTHUNDER (BT; PID 5015) and PID 5664 along with NIRSpec/IFU DDT PID 9433. In order to ensure homogeneity in the data, all spectra were processed with the JADES GTO pipeline (see Scholtz et al. 2026a for details). For the IFU data, we performed optimal aperture extraction to obtain 1D integrated spectra directly comparable to those from MSA. In addition, as the IFU data reduction pipeline generally underestimates uncertainties, we rescaled the errors on the 1D spectra by a ratio between the mean error and the rms of the continuum residuals in line-free parts of the spectra, finding that the IFU errors are generally underestimated by a factor of 2-3.

As the main goal of this work is studying the incidence rate of absorption features in the broad Hα line profiles of AGN, we only utilize R1000 and R2700 data. As RUBIES only utilized the F290LP/G395M grating, which covers $\lambda > 2.9$ μm, no AGN at $z < 3.4$ were selected from this survey. The procedure of selecting broad line emitters closely follows that of Juodžbalis et al. (2026a). We refit all spectra available, modelling the Hα line as a superposition of multiple Gaussians representing the narrow and broad Hα emission and the [N II] doublet. To select a source as a broad line AGN, we require the Bayesian Information Criterion (BIC $\equiv \chi^2 + k \ln n$, where k is the number of fitting parameters and n is the number of data points) to differ by > 10 between narrow-only and narrow+broad Hα models. In addition, we discard sources which have a broad component in [O III]λ5007 that is kinematically matched to what is seen in Hα, since for such objects, the broad line signal is likely produced by outflows. Unlike Juodžbalis et al. (2026a), we implement a stricter signal to noise[1] cut of 20 as below this threshold it becomes difficult to detect absorption features in the broad line profiles (see Section 3.1 for details). This selection procedure resulted in a parent sample of 38 AGN from the MSA surveys (20 from JADES, 17 from RUBIES and 1 from CEERS) as well as 9 additional sources from the IFU surveys that were not already covered by equivalent resolution MSA data, for a total of 47 targets, for which we performed a search of absorption features. In addition, we split the parent sample into LRD and non-LRD sources by employing the 'v' shape selection criterion consistent with that of Scholtz et al. (2026b); Brazzini et al. (2026):

[1] We define S/N as the ratio of the total line flux integrated within the line FWHM to the quadrature-combined error in the same range.

(i) $\beta_{UV} < -0.2$
(ii) $\beta_{opt.} > 0$

The slopes above were computed at rest-frame wavelengths of 1200–3600 Å for β_{UV} and 3700–7000 Å for $\beta_{opt.}$ respectively, masking the flux at the locations of strong emission lines such as Hα and [O III]$\lambda\lambda$4959,5007.

In total, 35 sources in the parent sample are identified as LRDs, with the remaining 12 mostly consisting of LBDs, with the exception of JADES-GN-209777 – a reddened quasar (Juodžbalis et al. 2026a, Ma, in prep.). This skew towards LRDs likely results from a combination of selection bias, as LRDs are easy to select photometrically. Historically LRDs were selected via stringent photometric cuts requiring very red optical continua (Hviding et al. 2025; Rinaldi et al. 2026). As a result, JWST spectroscopic surveys, such as RUBIES, were optimized to target bright red sources rather than the general AGN population. In addition, the LRD fraction appears to increase at higher AGN luminosities (Hainline et al. 2025).

While in the initial selection above, we approximated the BLR shape as a single Gaussian, high S/N data generally reveals the inherent non-Gaussianity of BLR profiles (e.g. Laor 2006; Rusakov et al. 2025). Indeed, for all of the parent sample sources, the single Gaussian fits leave considerable residuals in the wings of the line. Hence, when searching for absorbers, we employ three different more complex BLR models following the methods of Scholtz et al. (2026b):

- Double Gaussian (2G) – the line profile is modeled as a sum of two Gaussians with independent FWHM, but fixed redshift.
- Lorentzian (Lor) – the line profile is modeled as a Lorentzian distribution with FWHM, redshift and normalization left as free parameters.
- Electron scattering (Sct) – such a profile is produced by Thomson scattering off of free electrons and consists of a Gaussian core and exponential wings (Laor 2006; Rusakov et al. 2025). We model this profile as a Gaussian convolved with an exponential of the form:

$$E(\lambda) = e^{-|\lambda-\lambda_0|/W}, \tag{1}$$

where λ_0 is the central wavelength and W the width of the exponential.

We note that the detailed exploration of BLR shapes of our objects is beyond the scope of this work and was a topic of Brazzini et al. (2025, 2026); Scholtz et al. (2026b). Hence, in our final measurements, we characterized the best fit profiles by three parameters - redshift, total luminosity and total FWHM for self-consistent comparison between the best-fitting models.

The absorption features themselves were modeled assuming a Gaussian optical depth profile (Juodžbalis et al. 2024b):

$$\tau_\lambda = \tau_0 \exp\left[-0.5\left(\frac{\lambda - \lambda_0 e^{\Delta v/c}}{\sigma}\right)^2\right], \tag{2}$$

where τ_0 is the optical depth at the core of the line, Δv is the velocity shift of the absorber and σ is its velocity dispersion, coupled with a standard attenuation model:

$$f_\lambda = 1 - C_f + C_f e^{-\tau_\lambda}, \tag{3}$$

where C_f is the covering fraction of the absorbing medium.

The fitting was carried out utilizing Bayesian methods, with the posteriors sampled using the `emcee` sampler (Foreman-Mackey et al. 2013). We utilized uninformative uniform priors on most of the fitted quantities with the exception of narrow and broad line velocity shifts, which were constrained to be within 100 km s^{-1} and 500 km s^{-1} of the values determined by prior visual inspection respectively.

The absorbers were selected from the parent sample following the same ΔBIC method as the initial AGN selection, requiring absorber models to improve the BIC by more than 5 to be selected. This was followed by visual inspection of the selected targets to exclude any data artifacts masquerading as absorption features like cosmic ray hits causing single pixel downturns that automated fitting could flag as absorption. In addition, we visually inspected the remainder of the sample to ensure that no absorption features were missed by the fitting procedure. The preferred BLR model was likewise determined by the BIC criterion, however, in cases where multiple BLR models had ΔBIC < 5 relative to each other, the posterior samples of all acceptable BLR models were combined in estimating the final properties of the absorbers and broad line profiles. Hence, the uncertainties on the measurements of some of our sources are considerably higher - reflecting the degeneracies induced by competing BLR models.

The absorber selection procedure described above yielded 13 sources with robust detections of Hα absorption features from the parent sample (all of which are LRDs; Figure 1) which were subsequently used for estimating the absorber incidence rate. In addition to these targets, we also include additional independently discovered AGN with absorption features – The Cliff (de Graaff et al. 2025b), for which we use the R2700 IFU observations from DDT PID 9433(Ivey et al. 2026) and QSO1 (Furtak et al. 2024), which is a strongly lensed source that would be undetectable in field surveys, to boost the overall sample statistics by including the most BH*-like LRDs. Hence, the sample used to analyze absorber properties consists of a total of 15 targets. Aside from the main set of absorbers, we identify a tentative absorption feature in the spectrum of BT-G23-4286, while appearing robust in the raw aperture spectrum (Figure A2), the feature fails to pass the robustness criteria once the underestimated IFU errors are taken into account. Hence, we report the best fit values for BT-G23-4286, but do not include it in further analysis.

We also find that 9 of our sample sources show clear detections of corresponding Hβ absorption, which we fit with similar methods to that of Hα. The main measured Hα absorber properties for our targets are summarized in Table 1 while Table 2 shows the properties of Hβ absorbers. Figure 1 summarizes the classification of the parent sample into LRDs and LBDs and shows that only LRDs have absorption features. Some example Hα profile fits are shown in Figure 2, while the remainder are given in Figure A1. The Hβ fits for sources with Hβ absorbers are shown in Figure B1.

3 INCIDENCE RATE OF BALMER ABSORBERS

While previous studies already hinted at a high (> 20%) incidence rate of Balmer absorption in JWST-discovered AGN and LRDs in particular (Matthee et al. 2024; Juodžbalis et al. 2026a; Lin et al. 2026), more comprehensive assessments of this quantity are required. With a parent sample of 47 unique sources of which 13 show absorption signatures, we estimate an incidence rate of ∼ 28% for our entire sample of AGN, a 37% absorber incidence for LRDs and < 8% for LBDs. However, this number only represents a lower limit as a simple ratio does not account for inherent incompleteness of R1000 and R2700 data since narrow line infill can hide absorbers with velocities lower than the LSF as discussed in the following section.

ID	R.A. [°]	Dec [°]	z	BLR model	$\mathrm{FWHM}_{\mathrm{H}\alpha;\mathrm{br}}$ [km s^{-1}]	$L_{\mathrm{H}\alpha;\mathrm{br}}$ [$\times10^{43}$ erg s^{-1}]	$\sigma_{\mathrm{H}\alpha}$ [km s^{-1}]	$\tau_{0;\mathrm{H}\alpha}$	$C_{\mathrm{f;H}\alpha}$	$\mathbf{\Delta v_{H\alpha}}$ [km s^{-1}]	$\mathbf{EW_{0;H\alpha}}$ [Å]
Main sample											
JADES-GN-28074	189.06458	62.27382	2.260	Sct	1750^{+5}_{-6}	$2.514^{+0.006}_{-0.006}$	205^{+1}_{-1}	$1.28^{+0.02}_{-0.01}$	$0.994^{+0.004}_{-0.008}$	-425^{+1}_{-1}	$8.73^{+0.07}_{-0.07}$
DH-GS-5070	53.09200	-27.90314	3.642	2G	1785^{+14}_{-14}	$0.556^{+0.003}_{-0.003}$	107^{+3}_{-3}	$6.63^{+1.01}_{-0.74}$	$0.93^{+0.04}_{-0.06}$	-17^{+3}_{-3}	$10.59^{+0.44}_{-0.62}$
RUBIES-182791	34.21381	-5.08705	4.715	2G	1752^{+87}_{-96}	$0.740^{+0.015}_{-0.014}$	130^{+19}_{-24}	$5.41^{+2.97}_{-2.67}$	$0.42^{+0.06}_{-0.05}$	-298^{+48}_{-54}	$5.44^{+1.07}_{-0.92}$
BT-J1148†	177.05796	52.86280	5.011	2G	956^{+6}_{-6}	$0.542^{+0.003}_{-0.003}$	58^{+2}_{-2}	$4.25^{+0.58}_{-0.51}$	$0.52^{+0.02}_{-0.02}$	57^{+2}_{-2}	$2.78^{+0.08}_{-0.07}$
JADES-GN-68797†	189.22914	62.14619	5.040	Sct	2009^{+9}_{-11}	$5.443^{+0.017}_{-0.018}$	186^{+3}_{-3}	$1.91^{+0.02}_{-0.11}$	$0.984^{+0.012}_{-0.022}$	-215^{+6}_{-6}	$8.50^{+0.27}_{-0.31}$
JADES-GS-159717†	53.09753	-27.90126	5.078	2G,Sct	1617^{+67}_{-67}	$0.859^{+0.023}_{-0.023}$	109^{+7}_{-7}	$2.73^{+0.92}_{-0.92}$	$0.828^{+0.125}_{-0.125}$	-3.5^{+4}_{-4}	$6.54^{+0.39}_{-0.45}$
5664-GN-15498†	189.28554	62.28078	5.085	Lor	1162^{+10}_{-10}	$0.529^{+0.004}_{-0.004}$	67^{+3}_{-3}	$5.96^{+1.47}_{-1.12}$	$0.931^{+0.044}_{-0.053}$	-47^{+5}_{-5}	$6.10^{+0.26}_{-0.25}$
RUBIES-42046	214.79537	52.788847	5.276	Sct	2003^{+51}_{-53}	$4.866^{+0.071}_{-0.069}$	263^{+15}_{-15}	$2.03^{+0.53}_{-0.33}$	$0.928^{+0.050}_{-0.064}$	-284^{+32}_{-39}	$18.63^{+0.49}_{-0.52}$
5664-GS-13971†	53.13858	-27.79025	5.481	Lor,Sct	1384^{+185}_{-185}	$0.861^{+0.078}_{-0.078}$	100^{+13}_{-13}	$2.19^{+0.55}_{-0.55}$	$0.91^{+0.13}_{-0.13}$	-146^{+36}_{-36}	$6.31^{+0.22}_{-0.23}$
5664-GN-9771†	189.28100	62.24731	5.538	2G,Sct	2312^{+299}_{-299}	$5.492^{+0.276}_{-0.276}$	69^{+16}_{-16}	$1.66^{+1.58}_{-1.58}$	$0.466^{+0.51}_{-0.51}$	-199^{+57}_{-57}	$3.47^{+0.08}_{-0.08}$
JADES-GN-38147	189.27068	62.14842	5.869	2G	1675^{+55}_{-49}	$0.991^{+0.020}_{-0.019}$	72^{+27}_{-24}	$2.25^{+1.82}_{-1.10}$	$0.596^{+0.290}_{-0.129}$	-358^{+31}_{-23}	$3.72^{+1.02}_{-0.63}$
RUBIES-49140	214.89225	52.87741	6.686	2G	2475^{+46}_{-45}	$6.039^{+0.086}_{-0.079}$	124^{+13}_{-10}	$6.14^{+2.33}_{-1.86}$	$0.622^{+0.192}_{-0.129}$	3.7^{+12}_{-12}	$8.02^{+2.19}_{-1.64}$
RUBIES-2	214.98303	52.95600	6.984	2G	1922^{+41}_{-38}	$4.33^{+0.045}_{-0.045}$	74^{+5}_{-5}	$2.71^{+0.33}_{-0.33}$	$0.794^{+0.034}_{-0.028}$	-305^{+4}_{-5}	$5.45^{+0.18}_{-0.18}$
Additional sources											
The Cliff†	34.41075	-5.12966	3.549	Sct	865^{+2}_{-7}	$0.400^{+0.001}_{-0.002}$	92^{+1}_{-1}	$1.12^{+0.05}_{-0.04}$	$0.976^{+0.017}_{-0.025}$	70^{+1}_{-1}	$3.62^{+0.07}_{-0.06}$
A2744-QSO1†	3.57984	-30.40157	7.036	Lor	816^{+11}_{-10}	$0.149^{+0.02}_{-0.002}$	71^{+8}_{-7}	$4.66^{+2.24}_{-1.74}$	$0.268^{+0.032}_{-0.028}$	-28^{+5}_{-5}	$1.68^{+0.17}_{-0.17}$
Tentative absorber											
BT-G23-4286†	3.6192	-30.4233	5.840	2G	928^{+76}_{-21}	$0.352^{+0.083}_{-0.005}$	35^{+10}_{-4}	$2.75^{+1.35}_{-1.79}$	$0.51^{+0.31}_{-0.05}$	-140^{+7}_{-24}	$1.61^{+0.17}_{-0.13}$

Table 1. Table summarizing the broad Hα line and absorber properties. The first column indicates the object ID formed by adding the name or PID of the survey to the original catalog ID. Columns 2 and 3 give the R.A. and Dec respectively. Column 4 shows the redshifts inferred from the narrow lines. The following column lists the best fit BLR models with multiple models listed indicating comparable performance. Columns 6 and 7 list FWHM of broad Hα and its luminosity respectively. The remaining five columns list the absorber properties in order of Doppler broadening (σ), peak optical depth τ_0, velocity offset (Δv) and rest-frame equivalent width (EW_0). Hα absorber parameters in bold (Δv and EW_0) are more reliably constrained by our data than the others. Object IDs with † next to them indicate sources for which R2700 data was available.

ID	$\mathrm{FWHM}_{\mathrm{H}\beta;\mathrm{br}}$ [km s^{-1}]	$L_{H\beta;br}$ [$\times10^{43}$ erg s^{-1}]	$\sigma_{H\beta}$ [km s^{-1}]	$\tau_{0;H\beta}$	$C_{f;H\beta}$	$\mathbf{\Delta v_{H\beta}}$ [km s^{-1}]	$\mathbf{EW_{0;H\beta}}$ [Å]
Main sample							
JADES-GN-28074	3227^{+47}_{-46}	$0.173^{+0.003}_{-0.003}$	167^{+12}_{-13}	$2.12^{+0.75}_{-0.54}$	$0.888^{+0.077}_{-0.102}$	-234^{+31}_{-34}	$9.40^{+1.36}_{-1.33}$
DH-GS-5070	3299^{+395}_{-329}	$0.035^{+0.003}_{-0.003}$	125^{+33}_{-36}	$5.14^{+3.23}_{-2.98}$	$0.658^{+0.144}_{-0.129}$	-154^{+132}_{-133}	$7.23^{+2.72}_{-2.02}$
JADES-GN-68797†	2708^{+209}_{-200}	$0.244^{+0.017}_{-0.017}$	106^{+15}_{-18}	$5.77^{+2.89}_{-2.79}$	$0.786^{+0.131}_{-0.147}$	-146^{+87}_{-87}	$7.47^{+1.83}_{-2.36}$
RUBIES-42046	2692^{+250}_{-236}	$0.374^{+0.031}_{-0.030}$	153^{+40}_{-34}	$4.57^{+3.20}_{-2.00}$	$0.833^{+0.113}_{-0.123}$	-420^{+97}_{-94}	$11.54^{+2.39}_{-2.27}$
5664-GN-9771†	4385^{+66}_{-63}	$0.457^{+0.009}_{-0.009}$	93^{+7}_{-7}	$2.98^{+0.54}_{-0.44}$	$0.977^{+0.017}_{-0.029}$	-222^{+19}_{-19}	$6.84^{+0.56}_{-0.53}$
RUBIES-49140	3255^{+209}_{-199}	$0.596^{+0.034}_{-0.032}$	64^{+44}_{-33}	$4.27^{+3.56}_{-2.35}$	$0.664^{+0.187}_{-0.145}$	173^{+88}_{-96}	$4.26^{+3.31}_{-1.11}$
RUBIES-2	3716^{+186}_{-206}	$0.470^{+0.025}_{-0.022}$	63^{+42}_{-39}	$5.80^{+2.84}_{-2.69}$	$0.856^{+0.102}_{-0.150}$	-252^{+100}_{-100}	$5.39^{+4.98}_{-1.18}$
Additional sources							
The Cliff†	2804^{+123}_{-101}	$0.035^{+0.001}_{-0.001}$	167^{+12}_{-13}	$2.12^{+0.75}_{-0.54}$	$0.629^{+0.124}_{-0.083}$	264^{+51}_{-51}	$4.54^{+0.40}_{-0.48}$
A2744-QSO1†	2061^{+264}_{-238}	$0.013^{+0.006}_{-0.006}$	104^{+77}_{-37}	$3.61^{+3.93}_{-2.68}$	$0.312^{+0.188}_{-0.123}$	178^{+91}_{-101}	$2.22^{+1.36}_{-0.82}$

Table 2. Same as Table 1, but for sources with Hβ absorption.

3.1 Completeness simulations

In order to account for this incompleteness, we perform completeness simulations by fitting simulated broad Hα profiles and testing the recovery rates across the simulated parameter space. The broad Hα profiles were simulated to be single Gaussians with widths drawn from a uniform distribution spanning the range from 1000 to 7500 km s^{-1} – representative of the FWHM of the general JWST-discovered AGN population (Juodžbalis et al. 2026a). We note that adopting a more complex BLR shape affects the inferred absorber properties, but not the selection. The properties of the simulated absorption (τ_0, Δv, σ and C_f) were likewise drawn from uniform distributions with boundaries set according to the parameter space spanned by our sample of absorbers, albeit slightly extended to cover weaker features that may be missed even in deep R2700 observations. The assumed distributions were – $\Delta v \in [-800, 800]$ km s^{-1}, $\sigma \in [50, 300]$ km s^{-1}, $\tau_0 \in [0.8, 10]$ and $C_f \in [0.1, 1.0]$. The normalization of the broad emission line was sampled in flux space with $\log F_{\mathrm{BLR}} \in [-18, -15.5]$ erg s^{-1} cm^{-2}, corresponding to $\log L_{\mathrm{BLR}} \in [41, 43.7]$ erg s^{-1} at the median redshift of our sample ($z = 4$). This, coupled with parametrising the final completeness functions in terms of BLR S/N, ensures that the results are agnostic

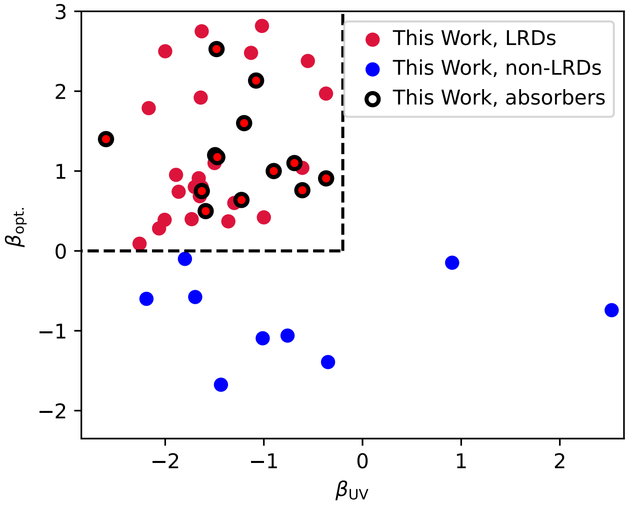

Figure 1. Showcase of the UV and optical slopes of the parent sample. The dashed lines denote the LRD region. Sources identified as LRDs are shown in red while LBDs - in blue. The objects with absorption features are highlighted with black edges. It can be seen that all absorbers lie in the LRD region.

to the redshift or noise level of the simulated sources. The narrow Hα flux was fixed to 50% of the BLR flux, consistent with the mean flux ratio for the parent sample sources. The [N II] line emission was drawn from a Gaussian distribution, ensuring that it is at least 1 dex fainter than the narrow Hα, consistent with what is seen in high redshift AGN (Maiolino et al. 2024b; Juodžbalis et al. 2026a).

We carry out the completeness simulations by convolving the simulated spectra with either R2700 or R1000 line spread functions (LSFs) and injecting Gaussian noise consistent with that of JADES Medium tier observations, since their 0.8 h exposure times per grating (Scholtz et al. 2026a) gives noise level comparable to that of the majority of our sample spectra. In addition, expressing the completeness function in terms of BLR S/N means that the exact value of the noise injected has little effect on our results. In total, we generated 150,000 simulated R1000 and R2700 spectra each. These spectra were then fit using bounded least squares minimization to make the fitting computationally tractable. We used entirely the same criteria for selecting absorbers from the simulated spectra as for the real data set, requiring $\Delta BIC > 5$ between the model without and the one with the absorber. However, as our simulations do not accurately model correlated NIRSpec noise and do not include data artefacts, we add an additional selection criterion for the simulated data. Namely, we require the absorption feature to have S/N > 5, defined similarly to the BLR S/N except that it is calculated for the feature remaining after subtracting the fitted emission. Accompanying completeness simulations, we fit similar sets of simulated spectra that do not include absorption features to quantify the potential contamination rates, that is, the fraction of sources with no absorption identified as absorbers.

We find that the contamination across both gratings is negligible and completeness drops off to below 50% for S/N < 20 for both R1000 and R2700 observations (Figure 3). The completeness function strongly depends on the absorber properties such as the velocity shift (Δv) as illustrated in Figure 3 and discussed in Section 3.3 (also demonstrated for a single object in D'Eugenio et al. 2026). In addition, R1000 performs substantially worse than R2700 in parameter recovery as shown by D'Eugenio et al. (2026) and discussed in more detail in the following section.

3.2 Parameter recovery tests

Before continuing towards further analysis of the demographics of the detected absorbers, we utilize the simulated data set to conduct parameter recovery tests in order to determine which parameters of Equation 2 and Equation 3 are recovered well in the fitting.

We define the deviation between the simulated 'real' and fitted values as the Euclidean distance between the simulated and estimated feature vectors. In order to ensure that each parameter is evenly weighted, we remap the four absorber parameters (Δv, σ, τ_0 and C_f) to dimensionless features spanning the same dynamic range using the following equation:

$$\theta_i = \frac{\vartheta_i - \bar{\vartheta}_i}{\max \vartheta_i - \min \vartheta_i}, \tag{4}$$

where ϑ_i is the original parameter while θ_i is the corresponding feature. The above remapping ensures that $\theta_i \in [-0.5, 0.5]$ for all θ_i. The deviation between the simulated and estimated feature vectors is then defined as follows:

$$D = \sqrt{\frac{\sum_{i=0}^{N} \left(\theta_i - \hat{\theta}_i\right)^2}{N}}, \tag{5}$$

where θ_i and $\hat{\theta}_i$ are the ground truth and fitted features respectively and N is the total number of features in the vector. Deviation defined this way maps to $D \in [0, 1]$ with zero representing perfect parameter recovery and one – a catastrophic failure.

We find that the R1000 grating performs significantly worse than R2700 when recovering the full 4-parameter absorber model (dashed lines in Figure 4). We quantify the difference between the D distributions using the Kullback–Leibler divergence (D_{KL}), finding that $D_{KL} = 0.17$ between the simulated R2700 and R1000 data sets with the mode of the distribution equal to 0.1 and 0.3 for R2700 and R1000 respectively. It should also be noted that both distributions have significant tails towards high D values with excess kurtosis values of 6 – 7, indicating a prevalence of catastrophic outliers. While this could partially be attributed to least-squares fitting being prone to getting trapped in local minima, the parameters defining the prominence of an absorption feature – σ, τ_0 and C_f, are intrinsically degenerate. We attempt to remove these degeneracies by coalescing the three aforementioned parameters into a single equivalent width measure:

$$\mathrm{EW}_0(1+z) = \int (1 - F_{obs}/F_{em})\, d\lambda \equiv \int C_f \left(1 - e^{-\tau_\lambda}\right) d\lambda, \tag{6}$$

where F_{obs} is the observed flux including the absorption feature, F_{em} - the total emission and z - the redshift of the source. The remaining parameters are the same as in Equation 2 and Equation 3. This reduces the total number of features from 4 to 2, reapplying the earlier analysis shows that the simplified feature vector is better recovered by both R2700 and R1000 data (Figure 4) with reduced catastrophic outlier rates (excess kurtosis of 1 – 3) and the peaks of the distributions shifted to $D = 0.05, 0.08$. The KL divergence between the performance of R1000 and R2700 likewise reduces to 0.07, indicating a much closer match in the performance of the two gratings. Hence, in subsequent analysis we focus on Δv and EW_0 as the main parameters of each absorber as these are considerably better recovered than the full model and similar performance of R1000 and R2700 gratings reduces the inhomogeneity in the measurement accuracy as only 17/47 of our targets have R2700 data.

Lastly, we note that the infill by the narrow Hα line causes unrecoverable degeneracies even in the high resolution data. In particular, such infill can make a broad rest-frame absorption feature appear narrower and redshifted. Hence, even the reduced feature vector is

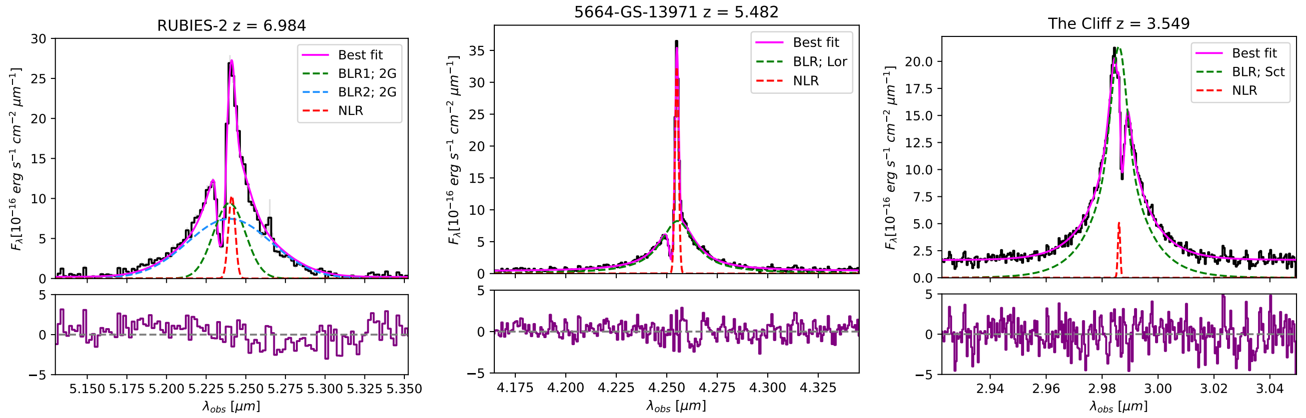

Figure 2. Example fits to the broad Hα absorbers in the sample. Left panel shows a source fit best by a double Gaussian, middle panel - Lorentzian profile and the right panel - electron scattering. The data is shown in black, with gray shading indicating errors, the best fit model is displayed in magenta. The dashed green line shows the BLR profile, the dashed blue line shows the second BLR component in case of a double Gaussian fit. The red line shows the narrow Hα. The panel below each Hα profile fit shows the best fit residuals. In case of two BLR models fitting equally well, we plot the absolute best one in terms of ΔBIC.

not recovered with perfect accuracy. Therefore, the absorber demographics of any JWST samples should be interpreted with caution.

3.3 Completeness corrected absorption incidence rate

Correcting the directly estimated incidence rate for incompleteness is a non-trivial task as a simple ratio will miss the intricacies introduced by the underlying distribution of absorber properties. For example, even if broad Hα is detected to high S/N and the absorption has a high intrinsic EW$_0$, the feature may nevertheless be missed if it is rest-frame ($\Delta v = 0$) and covered by the narrow Hα emission. Hence, we perform a parameter-aware completeness correction by first defining a completeness function from the simulated data as a function of the broad line S/N and the two absorber parameters – $C \equiv C(S/N, EW_0, \Delta v)$. This function was constrained by binning the simulated data in 3D bins of the three variables. As all of our sources with detected absorbers have $S/N > 60$, we are in the regime where C varies more with EW_0 and Δv rather than the brightness of the BLR (see Figure 3). Unfortunately, the small size of our sample makes 2D histograms prone to overbinning. Hence, we construct two 1D completeness functions varying with Δv and EW_0 respectively by averaging out the remaining two parameters, only considering regions where the parameters being averaged are within the range populated by our sample sources to avoid biasing the completeness. We thus perform two separate completeness corrections, checking for consistency between them.

With the 1D completeness functions in hand, we bin the absorbers sample in the same space as C and perform Bayesian inference to constrain the best-estimate on the incidence rate of Balmer absorption features together with a 95% credible interval (CI). The inference was performed on a per-bin basis utilizing the following formalism to infer the posteriors.

We denote the measured number of absorbers in the i-th bin as n_i, the completeness - C_i, the real number of absorbers is denoted by N_i, the parent sample size - M and the number of bins - B. The posterior is then defined by the standard Bayesian formula:

$$P(N_i|n_i) = \frac{P(n_i|N_i)P(N_i)}{P(n_i)}. \tag{7}$$

The likelihood function – $P(n_i|N_i)$, is then simply a binomial distribution with N_i as the number of trials and C_i as the success probability:

$$P(n_i|N_i) = \binom{N_i}{n_i} C_i^{n_i} \, (1 - C_i)^{N_i - n_i} \tag{8}$$

The prior, $P(N_i)$ is constructed to be uniform between $N_i = n_i$ and $N_i = M$. Marginalizing over the likelihood to obtain $P(n_i)$ then yields the following expression for the posterior:

$$P(N_i|n_i) = \frac{P(n_i|N_i)}{\sum_{N_i=n_i}^{M} P(n_i|N_i)} \tag{9}$$

We construct our best estimate for each bin by taking the most probable value given by the posterior, while the CI is defined to contain 95% of the posterior probability. We note that, while the above procedure does not automatically ensure that $\sum_i N_i \leq M$, we find that the completeness corrected source counts and their CIs automatically satisfy this constraint without it being imposed explicitly.

The final incidence rate is thus estimated as:

$$I = \frac{\sum N_{i;2700} + \sum N_{i;1000}}{M}, \tag{10}$$

we find that, for the combined sample of LBDs and LRDs, $I = 0.32$ (95% CI: 0.28 – 0.47) when using completeness defined with respect to Δv and $I = 0.30$ (95% CI: 0.28 – 0.45) when correcting with respect to EW_0. Both estimates and their CIs overlap within 2-3% and are hence functionally equivalent. We thus estimate that the incidence rate of absorbers, if LBDs and LRDs are treated as belonging to the same population, is $I \approx 31\%$ and no higher than 50%. However, this rate may still be underestimated if a significant fraction of absorbers occurs at rest-frame wavelengths where they can be hidden by the narrow Hα emission.

Splitting the sample into LRD and LBD sources results in an inferred $I = 0.44$ (95% CI: 0.38 – 0.65) for LRDs. While the latter value is somewhat lower than recent estimates by Matthee et al. (2026) and Lin et al. (2026), who report $\sim$ 60% and $\sim$ 65% incidence rates for high redshift and local LRDs respectively, these values are still consistent within our CI. The inferred incidence rate is high enough that the scenario in which effectively all LRDs have Hα absorption cannot be ruled out in light of narrow Hα infill effectively hiding rest-frame $|\Delta v| < 100$ km s^{-1} systems in R1000 data. On the other hand, no non-LRD sources in our parent sample display absorption features. Hence, we infer a 2σ upper limit on the incidence rate by

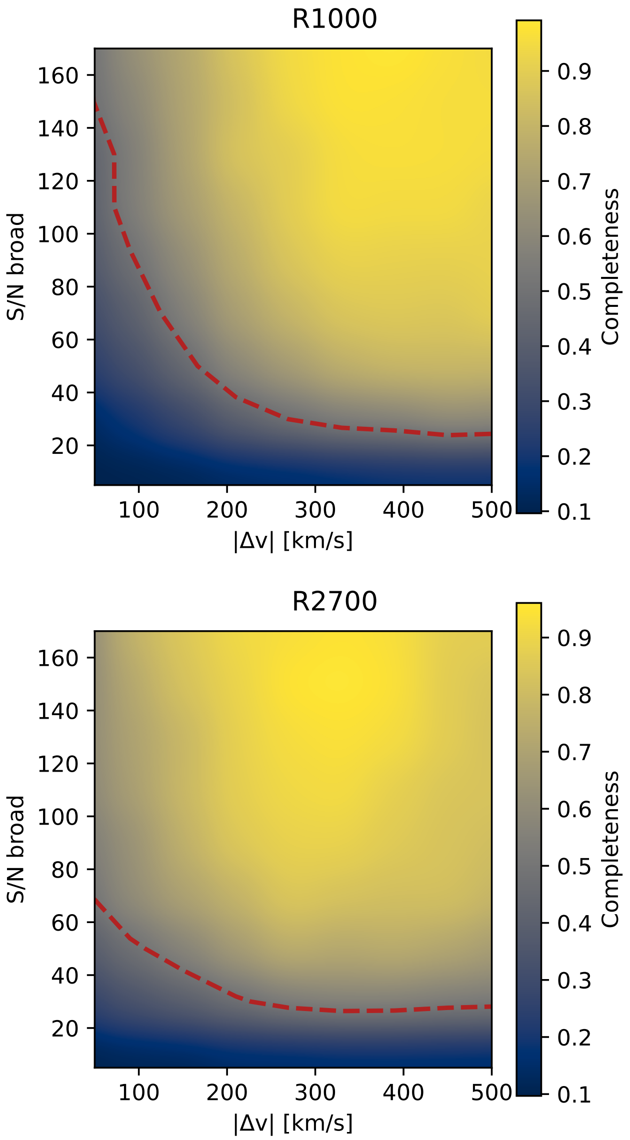

Figure 3. 2D completeness maps on the Δv – BLR S/N plane with the dashed lines indicating the 50% completeness threshold. Top panel shows the simulations for R1000, bottom – R2700. As can be seen here, the R1000 grating performs significantly worse than R2700 for $|\Delta v| < 200$ km s^{-1}.

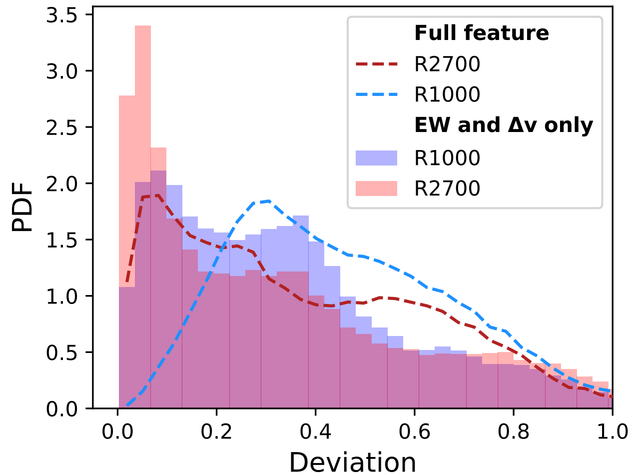

Figure 4. The distribution of deviation, as defined in Equation 5, for the simulated R2700 and R1000 data when considering the full feature vector (dashed lines) and the simplified version including just EW_0 and Δv (histograms).

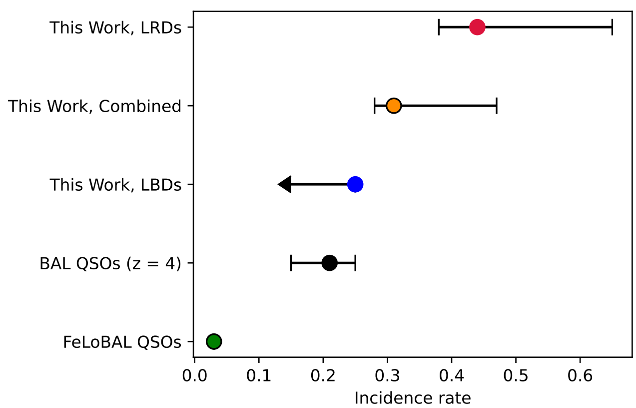

Figure 5. Comparison between Balmer absorption incidence rates for our sample populations and those of BAL and FeLoBAL QSOs (Leighly et al. 2025; Bischetti et al. 2023). The colored points show the best estimates while the black error bars represent the 95% Credible Intervals. As no LBDs in our sample have absorption features, their estimate is an upper limit.

assuming the same absorber distribution as seen for LRDs. Depending on whether the completeness is defined with respect to Δv or EW_0, the incidence of Balmer absorption in LBDs is $I < 0.08 - 0.25$ and conservatively we adopt the higher value. The comparison between our estimated Balmer absorption incidence rates and that for FeLoBAL QSOs (Leighly et al. 2025) is shown in Figure 5. As can be seen there, the JWST-discovered AGN population taken as a whole has a significantly higher incidence rate of Balmer line absorption than FeLoBAL QSOs (30% vs 0.3%). On the other hand, the Balmer absorbers appear to be a defining feature of LRDs with no LBDs in our sample displaying hydrogen absorption. Nevertheless, the conservative $I < 25\%$ upper limit for LBDs leaves significant room for a high absorber occurrence with larger sample sizes required to see if this absorption is truly absent in LBDs. We also note that, while FeLoBAL QSOs, which display prominent Balmer absorption are rare, the overall BAL fraction strongly evolves with redshift and reaches 50% at $z = 6$ (Bischetti et al. 2023). While the overall BAL fraction at the median z of our sample is lower ($\sim 20\%$), it is still considerably closer to the inferred incidence rates for our sample AGN (Figure 5). Therefore, it is reasonable to suggest that LRDs and BAL QSOs may be shaped by similar physical processes, yet occurring at different luminosities.

4 BALMER ABSORPTION DEMOGRAPHICS

Having explored the overall incidence rates of Hα absorption, we move to examining the demographics of our absorber sample. As only Δv and EW_0 are recovered well in R1000 and R2700 data, these are the main quantities on which we focus in the following analysis.

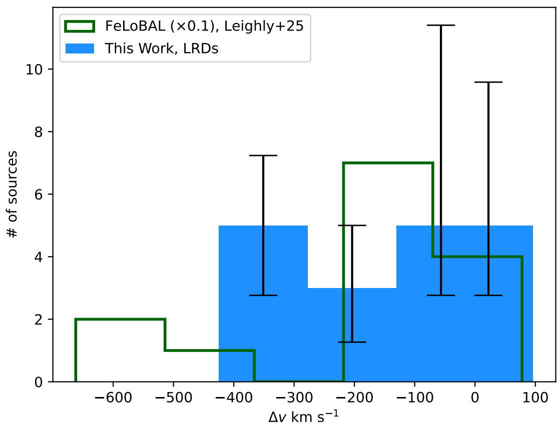

Figure 6. Velocity distribution of the sample absorbers when compared to FeLoBAL QSOs from Leighly et al. (2025), whose velocities were scaled down by a factor of 10 (green). The blue histogram shows the fiducial estimate while the black errorbars represent the 95% confidence intervals combined in quadrature with Poissonian counting error.

4.1 Absorption velocity distribution

The completeness corrected Δv distribution of our absorber sample is presented in Figure 6. As shown there, the absorption features are either at systemic redshift ($|\Delta v| < 100$ km s^{-1}) or significantly blue shifted ($\Delta v < -200$ km s^{-1}). Given that $C(\Delta v)$ is symmetric around $\Delta v = 0$, this asymmetry in the velocity distribution can not be accounted for by completeness effects alone. Hence, the dense media blanketing LRDs are generally weakly outflowing with median $\Delta v \approx -100$ km s^{-1} and largest blueshifts approaching -400 km s^{-1}. This argues against scenarios invoking quasi-static gas envelopes such as the BH* model (Naidu et al. 2025) as atmospheric pulsations possible in such environments would produce roughly equal amounts of outflowing or inflowing absorbers.

Nevertheless, the preponderance of absorbers within 100 km s^{-1} of the Hα rest-frame together with all absorber FWHM < 600 km s^{-1} may suggest that the absorbing gas is not tracing escaping high velocity outflows – in comparison, [O III] outflows in AGN generally exceed FWHM = 1000 km s^{-1} (Escott et al. 2025). While the Hα absorption is only tracing the densest parts of the outflowing gas, it is interesting to note that only two of our objects have any indication of large scale ionized outflows traced by the [O III]$\lambda\lambda$4959,5007 doublets (Figure B1). This would tentatively support a scenario in which LRDs represent a phase of AGN accretion in which the BH is surrounded by a dense medium, which prevents outflows from breaking out into lower density ISM, causing an abundance of dense gas absorption and a dearth of ionized outflows. In addition, the Hα outflow velocities in our sample resemble those of 'warm absorbers' found in ~ 50% of Seyfert 1 galaxies (Elvis 2000; Blustin et al. 2005). These warm absorbers generally share the $\Delta v \sim 100 - 300$ km s^{-1} velocity scale of LRDs, yet their lower densities mean that they are highly ionized and do not appear in Hα, suggesting that the outflowing gas seen in LRDs may be the high density counterpart of warm absorbers. However, our current sample is small, hence dedicated studies are required to establish a connection between the presence of Hα absorption and lack of outflows in the forbidden lines along with the relation between dense Hα absorption in LRDs and warm absorbers seen in Seyfert 1s.

Interestingly, the BAL QSOs that display Balmer absorption (the FeLoBALs) have a qualitatively similar velocity distribution (Figure 6) with some sources clustering around $\Delta v = 0$ plus a significant population of outflowing Hα absorbers. The velocity scales for Balmer absorption in FeLoBALs are greater by about a factor of 10, with $-6000 < \Delta v < 1000$ km s^{-1} compared to $-400 < \Delta v < 100$ km s^{-1} for our LRDs. However, the median bolometric luminosity of FeLoBALs from Leighly et al. (2025) is ~ 100 times greater than for our LRD sample ($10^{45.1}$ vs 10^{47} erg s^{-1}). Taking a simple assumption of radiation-driven outflows for which the kinetic energy injected into gas surrounding the central engine is proportional to the luminosity of the source, we would naively expect $L_{\rm bol} \propto \Delta v^2$. Hence, a 2 dex difference in luminosity would naturally produce a 1 dex difference in velocity. Therefore, it is possible that the Balmer absorption in LRDs is a physically similar phenomenon to that of FeLoBALs except occurring on lower energy scales.

4.2 Equivalent widths and column densities

Having discussed the Δv properties, we move on to the second parameter well constrained by our data - the EW$_0$. We find that our absorber sample spans a wide range of equivalent widths - from 1 to 15 Å. Considering that Hα absorption EW_0 traces the same n = 2 hydrogen required for a Balmer break, we investigate the relationship between these two parameters in our sample to investigate whether the Balmer breaks in our sample are produced by the same gas as the Hα absorbers as postulated by the BH* models (Ji et al. 2025a; Naidu et al. 2025).

We define the Balmer break strength as the flux ratio $F(4000Å)/F(3600Å)$, tracing the optical and UV continua right below and above the break wavelength (3646 Å), respectively. For comparison with the BH* model predictions, we use the synthetic BH* spectra library from Liu et al. (2026), who model LRDs as BHs encased in optically thick star-like atmospheres with low surface gravity and T_{eff} = 4000–6000 K. As shown in Figure 7, our sample sources have considerably weaker Balmer breaks and higher EW$_0$ values than predicted by the Liu et al. (2026) models with no apparent correlation between the two quantities. A potential explanation of this observation is that the UV and optical continua have different origins. If the UV emission originates from the host's stellar population or extended nebular emission, the infill would cause an underestimation in Balmer break strength and decorrelate the break and EW$_0$ measurements. Indeed, as shown by Sun et al. (2026), a large fraction of LRDs resemble pure BH* with extreme Balmer breaks under the assumption that [O III] and the UV continuum originate from the host environment.

Nevertheless, models proposing identical origins for the UV and optical continua (Lin et al. 2025; Asada et al. 2026) can not be discounted either. We investigate the parameter space spanned by single cloud CLOUDY models constructed in a similar way to those used in Juodžbalis et al. (2024a). Considering that the CLOUDY grids, unlike the BH* models, are not constrained to $C_f = 1$, we find that our measurements overlap well with a grid of high ionization ($\log U > -1.5$), high column density ($\log N_H/{\rm cm}^2 > 22$) and moderate turbulence (20 km s^{-1} < v_{turb} < 120 km s^{-1}) models (Figure 7). These results suggest that the EW$_0$ properties of LRD absorption features may be the result of a diverse set of conditions within the absorbing medium rather than radially symmetric stellar atmosphere-like configurations. Considering that the Δv distribution shown in Figure 6 is skewed towards blueshifted absorbers, this latter interpretation is likely more reasonable as there is little indication that the absorption features reside in stable systems. This interpretation favors the models of

Madau & Maiolino (2026a,b), which model the LRD Hα profiles as a combination of absorption and BLR stratification effects. However, multi epoch observations of absorber variability are needed before strong conclusions can be drawn.

As the EW_0 values are well recovered by both R1000 and R2700 data, we can obtain reasonable estimates of the column density of n = 2 hydrogen ($N_H(n = 2)$). We measure $N_H(n = 2)$ by the apparent optical depth method (Wang et al. 2024; Savage & Sembach 1991):

$$N_H(n = 2) = \frac{m_e c}{\pi e^2 f_0 \lambda_0} \tau, \tag{11}$$

where τ is the integrated line optical depth, λ_0 is the rest-frame wavelength of the Hα transition and f_0 its oscillator strength. Since the above equation integrates Equation 2 to get τ, it is unaffected by the degeneracy between τ_0 and σ and most of our sample sources have inferred $C_f > 0.5$. Hence, the $N_H(n = 2)$ is unlikely to be overestimated by more than 0.5 dex. We find that our LRDs sample spans $\log N_H(n = 2)/\mathrm{cm}^{-2}$ from 14 to 15, consistent with the total N_H values of $> 10^{22}$ cm^{-2} inferred for our LRDs (Figure 7) and individual sources (Juodžbalis et al. 2024b; Wang et al. 2024; D'Eugenio et al. 2025). Interestingly, LRDs appear as a low luminosity extension of FeLoBALs on the $N_H(n = 2) - L_{\mathrm{bol}}$ plane (Figure 8), with LRDs occupying the low luminosity - high $N_H(n = 2)$ quadrant, similar to NGC 4151, a local Seyfert 1 AGN with observed Balmer absorption (Anderson & Kraft 1969). Notably, however, weak anticorrelation between $N_H(n = 2)$ and L_{bol} seen in FeLoBALs is not reflected in LRDs. The relation instead appears to flatten out at low L_{bol}. Hence, while both LRD and BAL QSO absorbing environments are likely similar, LRDs appear to maintain higher columns of excited hydrogen, potentially due to smaller spatial scales and higher overall gas densities involved.

4.3 Sample correlations

Considering the earlier discussion on the problems of parameter recovery as well as the small sample size, we proceed cautiously when looking for correlations between the absorber parameters. Mainly, we perform jackknife resampling to ensure that any observed correlations are not driven by singular outliers. In addition, we bootstrap the errors on each measured quantity and only keep the correlations for which $p < 0.05$ after the earlier tests. We utilize the Spearman rank correlation as the main metric as it makes the least amount of assumptions about the properties of the underlying data set, only reporting correlations with $|\rho_r| > 0.5$.

Only two non-trivial correlations related to the observed absorption features survive the above procedure - the Δv of Hα and Hβ lines are strongly correlated (Figure 9) and we identify a noticeable anticorrelation between $L_{[\mathrm{OIII}]}$ and Δv of Hα with more [O III] luminous systems hosting more blueshifted absorbers (Figure 9). The correlation between $\Delta v_{\mathrm{H}\beta}$ and $\Delta v_{\mathrm{H}\alpha}$ is expected as these lines likely originate from the same gas. However, linear regression, performed with bootstrapped errors, shows that the relation between these two quantities significantly deviates from a 1:1 relation, with slope $m = 0.52^{+0.11}_{-0.09}$ and intercept $b = -105 \pm 15\ \mathrm{km\,s^{-1}}$. This suggests higher order effects present in the data - as discussed before, at least part of the deviation can be attributed to the limitations of JWST spectroscopy. However, the lack of any appreciable correlation between the EW_0 of Hα and Hβ absorbers strongly points towards partial covering playing a significant role in these systems. Partial covering ($C_f < 1$) would enable absorption to approach saturation without reaching zero flux causing apparent optical depths to deviate from the ratios set by relative oscillator strengths (Leighly et al. 2019), erasing the correlation expected from atomic physics alone. This was already demonstrated in observations of individual LRDs (D'Eugenio et al. 2025) and shown for low redshift FeLoBALs and LRDs alike (Leighly et al. 2025; Lin et al. 2026). Aside from partial covering, lack of EW_0 correlation is also expected if the absorption arises in the same clouds as the broad line emission. In this case, the Hα and Hβ transitions probe different cloud depths and are subject to different emission infill as expected in a stratified BLR (Li et al. 2017; Rakić 2022).

The correlations between $\Delta v_{\mathrm{H}\alpha}$ and narrow line luminosities are more unexpected - the location of the absorber is generally thought to be located at < 2 pc from the central ionizing source (Juodžbalis et al. 2024b; Naidu et al. 2025; Matthee et al. 2026), corresponding to the BLR scale, while narrow line emission, whether powered by the host or AGN, is generally found to be extended to scales of 100–1000 pc for both LRDs and regular Seyfert galaxies (Maiolino et al. 2026; Bennert et al. 2006; Zanchettin et al. 2023; Ishikawa et al. 2026). Hence, if the velocity offset and narrow line emission are both driven by energy injection from the central source, we would expect accompanying strong correlations between Δv and broad Hα luminosity, which do not appear in our sample. We thus investigate whether either UV or optical continuum luminosity at 1350 and 5100 Å respectively, correlates with $\Delta v_{H\alpha}$. We measure the respective luminosities from the prism spectra of our sample sources - overall 12 targets had the required prism coverage at 1350 Å and 13 at 5100 Å. We find no significant correlation between $\Delta v_{\mathrm{H}\alpha}$ and L_{5100} ($p > 0.05$, $\rho_r = -0.2$). On the other hand, we find a correlation between $\Delta v_{\mathrm{H}\alpha}$ and L_{1350} that is robust to outliers with $\rho_r = -0.61$ and $p = 0.046$, Figure 10. However, the relative faintness of LRD UV emission means that L_{1350} measurements are considerably less precise, hence $p = 0.14$ once the measurement errors are taken into account. Therefore, while the correlations between $L_{[\mathrm{OIII}]}$, $\Delta v_{\mathrm{H}\alpha}$ and L_{1350} are consistent with a common mechanism driving the UV, line emission and the outflow velocity, more precise measurements and larger samples are needed for a robust correlation analysis.

The tentative nature of the current correlation analysis of Balmer absorbers is reflected by the fact that we do not recover the reported tight correlation between $\Delta v_{\mathrm{H}\alpha}$ and Balmer break strength reported in Matthee et al. (2026) despite a 50% sample overlap and the slightly larger statistics of our sample (15 versus 12 absorbers). While it is possible that this discrepancy stems from differing assumptions regarding the BLR profile shapes made by Matthee et al. (2026), who fit all of their targets with the electron scattering model, we do not recover the Matthee et al. (2026) correlation even when fitting all sources with electron scattering profiles. Notably, Lin et al. (2026) also do not observe correlations between Δv and Balmer break strength. However, the currently small sample sizes and resolution-limited nature of the measurements, which are mostly taken at $R < 2000$, imply that any correlations reported on current LRD samples should be considered preliminary and subject to confirmation. Therefore, we do not draw strong conclusions from the correlations observed in our sample.

5 DISCUSSION

5.1 Are LRDs faint FeLoBAL QSOs?

Throughout the previous section, a common trend emerges of LRDs appearing as a low luminosity extension of the FeLoBAL QSO (FeLoBAL) population. This was already noted by Leighly et al. (2025), who point out that FeLoBALs share the reddened rest-frame

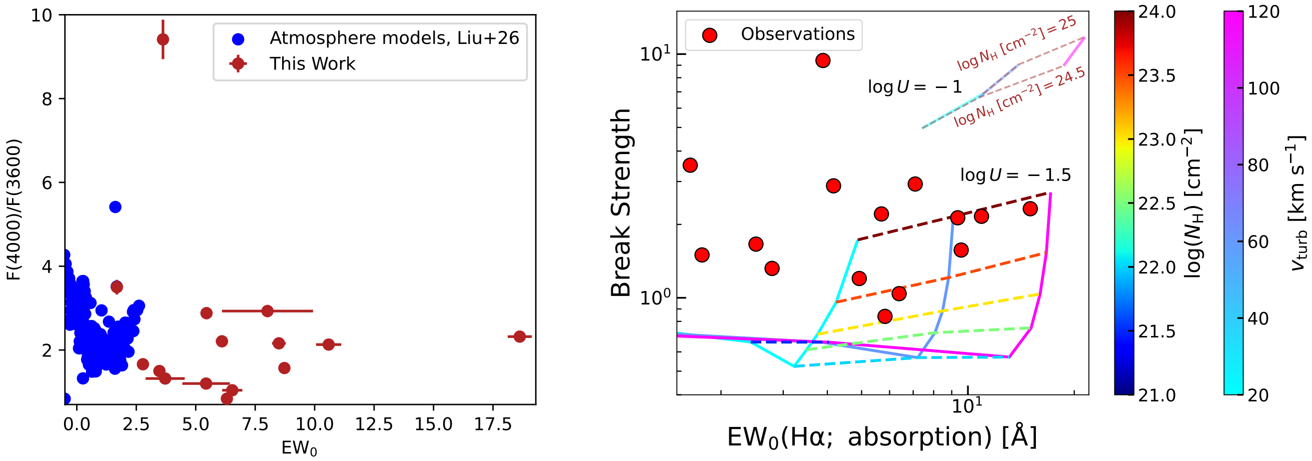

Figure 7. Left: Comparison between Balmer break strengths and EW_0 of our sample sources and stellar atmosphere models of Liu et al. (2026) showcasing the clear mismatch between our measurements and theoretical predictions of the BH* framework. **Right:** Showcase of example `CLOUDY` model grids computed at a fixed $\log U = -1.5$ and spanning the full range of N_H and v_{turb} values considered plotted over the same measurements as the left panel. Higher U and/or higher N_H would have the effect of moving the whole grid upwards as shown by the smaller model grid, and lower v_{turb} or lower C_f would move the grid to the left (see also Ji et al. 2025a), hence covering the entire observed parameter space.

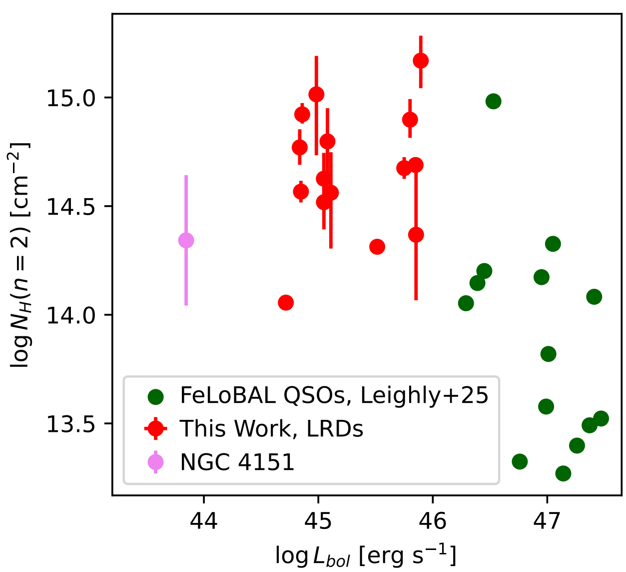

Figure 8. Comparison between our sample LRDs (red points) and FeLoBALs from Leighly et al. (2025) (green points) on the $N_H(n=2) - L_{\rm bol}$ plane. The violet circle illustrates the position of NGC 4151 - a prototypical local Seyfert 1 AGN with prominent Balmer absorption features (Anderson & Kraft 1969). As can be seen here, the LRDs show up as an extension of the BAL population, occupying the low luminosity, high column density region.

optical SED and X-ray weakness of LRDs. In addition, the broad Hα profiles of LRDs and FeLoBALs are qualitatively similar (Figure 11). Hence, it is tempting to assume a unified LRD - QSO framework at play. However, lower luminosity and higher obscuring column densities are not the only areas where LRDs differ from FeLoBALs. While an in-depth comparison study is beyond the scope of this work, in this section we will discuss the similarities and differences between LRDs and FeLoBALs observed so far.

The most notable difference between LRDs and FeLoBALs is a lack of permitted Fe II emission and absorption, which is ubiquitous in FeLoBAL systems (Choi et al. 2022; Leighly et al. 2025). LRDs instead, appear to display forbidden optical [Fe II] emission (Ji et al. 2025b; D'Eugenio et al. 2025) with only hints of Fe II absorption and permitted FeII emission (Ji et al. 2026) in the UV (D'Eugenio et al. 2025); see also the stacks in Pérez-González et al. (2026). Hence, the different iron emission patterns across LRDs and FeLoBALs can not be entirely the result of iron deficiency in the former. Intriguingly, high Balmer continuum optical depths can efficiently destroy Fe II emission in the UV (Netzer & Wills 1983; Wills et al. 1985), suggesting that Fe II emission may be suppressed by the same gas that is producing Balmer absorption. However, the increased collisional excitation in such environments would, in turn, predict strong optical FeII emission (Netzer & Wills 1983), which is absent in LRDs and other faint AGN (Trefoloni et al. 2025). This suggests that lower metallicity of the absorbing gas may be a factor suppressing the optical Fe II bump in LRDs. This is not immediately inconsistent with the detections of forbidden optical and permitted UV FeII emission in LRDs as optical [Fe II] can be efficiently produced by shocks (Knop et al. 1996), while the lines seen in the UV can be produced by Lyα fluorescence (Ji et al. 2026). Hence, significant further theoretical work is required to complete the picture of iron emission patterns in LRDs and establish the driving mechanisms behind the discrepancy with luminous QSOs.

Both LRDs and FeLoBALs display X-ray weakness. However, this weakness is considerably more pronounced in LRDs with only two high redshift 'X-ray dots' known so far (Hviding et al. 2026; Geris et al. 2026) along with one low redshift source (Lin et al. 2025; Ji et al. 2025b), while the remainder of the population shows no X-ray detections. This results in an $L_{\rm bol}/L_{[2-10{\rm keV}]}$ ratio in stacked X-ray data exceeding 10000 (Maiolino et al. 2025; Geris et al. 2026). In contrast, FeLoBALs are more consistently X-ray detected and display more modest, yet still significant, X-ray weakness with observed $\langle L_{\rm bol}/L_{[2-10{\rm keV}]}\rangle \sim 1700$ (Liu et al. 2018; Vito et al. 2018) and X-ray spectra consistent with obscuration by $N_{\rm H} \sim 10^{23}$ cm^{-2} media (Morabito et al. 2011; Rogerson et al. 2011). Considering the ~1 dex

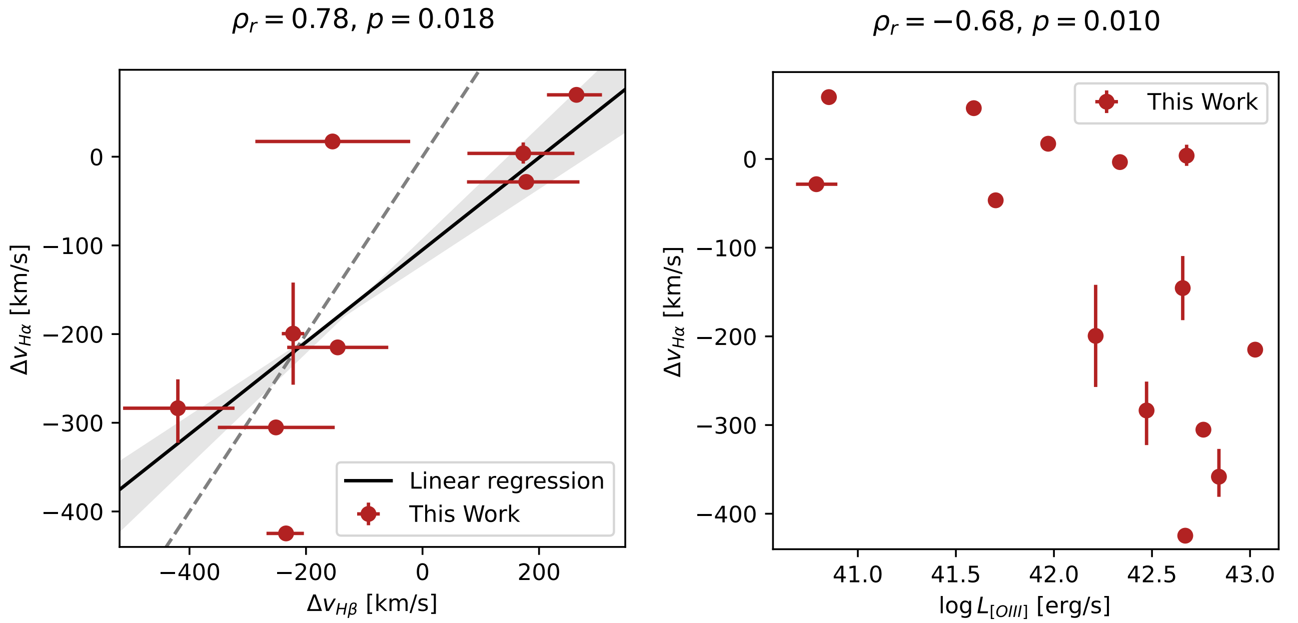

Figure 9. Left: The observed correlation between $\Delta v_{H\beta}$ and $\Delta v_{H\alpha}$. The data is shown in red, the best-fit linear regression with slope $m = 0.52^{+0.11}_{-0.09}$ and intercept $b = -105 \pm 15$ km s^{-1} is shown as a black line with gray shading indicating the uncertainties. The 1:1 relation is indicated by a dashed gray line. **Right:** Correlation between $\Delta v_{H\alpha}$ and $L_{[OIII]}$. The notation is the same as in the left panel except we do not attempt linear regression as we do not expect the data points to follow a linear relation.

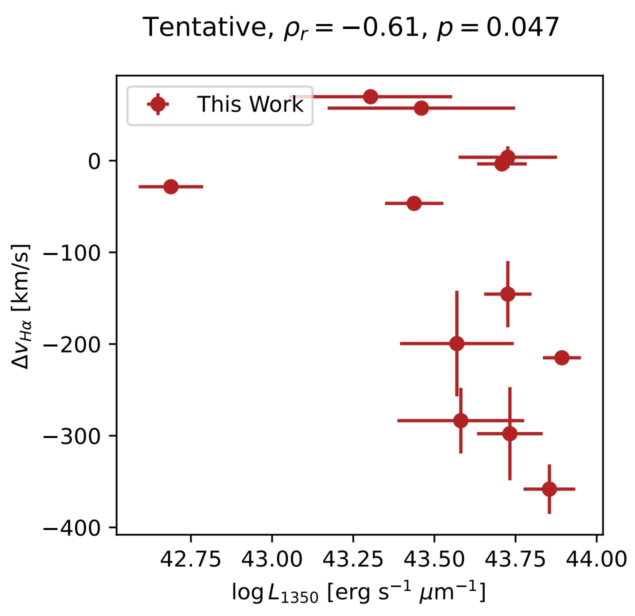

Figure 10. The tentative correlation between $\Delta v_{H\alpha}$ and L_{1350}. While the p-value is robust to outliers, the measurement errors give $p = 0.13$.

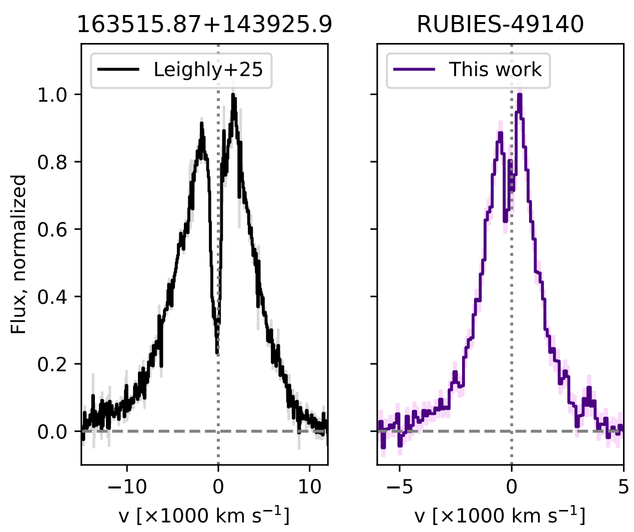

Figure 11. A qualitative comparison of broad Hα profiles of FeLoBAL SDSS 163515.87+143925.9 from Leighly et al. (2025) and one of our LRDs, RUBIES-49140 (also known as 'Irony', D'Eugenio et al. 2025). The horizontal dashed line denotes the zero flux threshold while the dotted vertical line marks the rest-frame velocity. It can be seen that, despite a factor of two difference in velocity scale, the FeLoBAL and Irony share a near rest-frame absorber and similar Hα profile shapes, including the slight asymmetry apparent at larger velocities.

higher $N_{\rm H}(n = 2)$ densities in LRDs, it is reasonable to suggest that the corresponding higher obscuration drives the greater X-ray weakness in these sources. However, LBDs are similarly X-ray weak while lacking the Balmer absorption features of LRDs. Therefore, the difference in the configuration or accretion properties of the central engines can not be discounted as the root cause of greater X-ray weakness in LRDs when compared to FeLoBALs.

In terms of bolometric luminosities and column densities, however, LRDs appear to strongly resemble the lower luminosity counterparts of FeLoBALs. In particular, they appear as a natural extension of the FeLoBAL population on the $L_{\rm bol} - N_{\rm H}(n = 2)$ plane (Figure 8). We investigate this resemblance further by comparing the energetics of outflows traced by LRD and FeLoBAL absorbers in the following section.

5.2 Absorber geometry and energetics

Motivated by the picture revealed by Figure 8, we explore deeper the apparent connections between the LRD/FeLoBAL absorber properties and the bolometric luminosities of the sources. We frame our discussion in terms of a simple toy outflow model following the formalism of Marconi et al. (2008) described below.

We consider a single geometrically thin spherical shell (or shell fragment) of hydrogen at a distance R from the accreting BH with a mass $M_{\rm BH}$ and bolometric luminosity L. The shell has a number density of n_H, thickness of ΔR (column density $N_H \equiv \Delta R n_H$), a covering factor C'_f and a radial velocity of v. We note that the covering factor here represents the covering as seen from the central source, hence it is not necessarily the same as in Equation 3, which is sensitive to the covering from the view of the observer.

The radiative force acting on a shell is given by:

$$F_{\rm rad} = \frac{LC'_f}{c}\int_0^\infty L_\nu(1 - e^{\tau_\nu})d\nu = \frac{LC'_f}{c}(1 - e^{\tau_{eff}}), \quad (12)$$

where L_ν and τ_ν are the frequency dependent monochromatic luminosity and optical depth respectively. The effective optical depth ($\tau_{\rm eff}$) can be approximated as $\tau_{\rm eff} = \sigma_{\rm eff} N_H$, where $\sigma_{\rm eff}$ is the effective luminosity-weighted interaction cross section per hydrogen nucleus. Further assuming that the absorber retains a constant physical area ($A = 4\pi R^2 C'_f = const.$) while expanding and does not undergo significant lateral expansion or fragmentation such that $\tau_{\rm eff}$ and N_H are constant. The absorber mass is then constant and given by:

$$m = AN_H\mu m_p = 4\pi R^2 C'_f N_H \mu m_p, \quad (13)$$

where μm_p is the mean mass per hydrogen nucleus. The final expression for $F_{\rm rad}$ thus becomes:

$$F_{\rm rad}(R) = \frac{LA}{4\pi c R^2}\left(1 - e^{-\tau_{\rm eff}}\right), \quad (14)$$

and therefore has the same R^{-2} dependence as the gravitational force,

$$F_{\rm grav}(R) = \frac{GM_{\rm BH}m}{R^2}. \quad (15)$$

The force balance on the shell can thus be expressed as a ratio between $F_{\rm rad}$ and $F_{\rm grav}$:

$$\Gamma_{\rm eff} \equiv \frac{F_{\rm rad}}{F_{\rm grav}} = \frac{L\left(1 - e^{-\tau_{\rm eff}}\right)}{4\pi G M_{\rm BH} c N_H \mu m_p}. \quad (16)$$

As both N_H and τ_{eff} are assumed to remain constant, $\Gamma_{\rm eff}$ is independent of radius. The net energy of the absorber is then given by:

$$E = \frac{1}{2}mv^2 - \frac{GM_{\rm BH}m}{R}\left(1 - \Gamma_{\rm eff}\right). \quad (17)$$

The form of Equation 16 and Equation 17 together prevent imposing exact force balance ($\Gamma_{\rm eff} = 1$) together with a parabolic escape trajectory ($E = 0$) for individual configurations. However, we interpret the observed distribution of absorber velocities, clustered around $\Delta v = 0$ with a modest excess at $\Delta v < 0$ (Figure 6), as qualitatively suggesting that at least part of the absorber population may lie close to the transition between gravitationally bound and radiatively accelerated configurations with $\langle\Gamma_{\rm eff}\rangle = 1$. If the characteristic absorber velocity scales with the gravitational velocity ($v^2 \propto GM_{BH}/R$), the force balance condition implies the following scalings between L and absorber properties depending on whether the shell is optically thick or thin:

$$L \propto \begin{cases} N_H v^2 R \text{ if } \tau_{\rm eff} \gg 1 \\ v^2 R \text{ if } \tau_{\rm eff} \ll 1 \end{cases} \quad (18)$$

The above expression has no explicit dependence on the covering factor C'_f and M_{BH}.

We can construct the products in Equation 18 from our measurements of $N_H(n = 2)$ (assuming $N_H(n = 2) \propto N_H$) and identifying the v in Equation 18 with Δv. While neither our nor Leighly et al. (2025) measurements can constrain R, we proceed under the assumption that LRD and FeLoBAL outflows have similar physical scales, which is consistent with current (albeit extremely uncertain) observational estimates of $R \sim 2$ pc for LRDs (Juodžbalis et al. 2024a) and 0.7 ± 0.5 kpc for FeLoBALs (Sharma et al. 2025). In addition, we note that the existence of a scaling relation between radius and luminosity ($R \propto L^\alpha$) would have the effect of flattening the slope of unity predicted by Equation 18 to $m = \frac{1}{1-\alpha}$. We estimate the L_{bol} of our LRDs using the calibrations from Stern & Laor (2012), which state $L_{bol} = 130 L_{H\alpha}$. While some recent results have raised doubts about the applicability of this scaling to LRDs (Greene et al. 2026), we note that their findings have been put in question by more recent results (Sok et al. 2026; Geris et al. 2026; Ji et al. 2026; Tang et al. 2026). In addition, our results hold even if we use $L_{H\alpha}$ directly, which we checked by converting the reported FeLoBAL L_{bol} to $L_{H\alpha}$ via the Stern & Laor (2012) relation. Hence, we use $L_{H\alpha}$ and L_{bol} as proxies for L interchangeably in the following analysis.

Utilizing the mean $N_H(n = 2)$ and $|\Delta v|$ from Leighly et al. (2025) FeLoBAL sample and our LRDs (Table 3), we obtain a ratio of $(N_H \Delta v^2)_{LRD}/(N_H \Delta v^2)_{BAL} = 0.04$. This is in almost exact correspondence to the ratio of the mean bolometric luminosities with $\langle L_{LRD}\rangle/\langle L_{BAL}\rangle = 0.039$. While at first glance this might suggest that the absorbing shells must be optically thick, the results of Section 4.1 show that Δv^2 appears to likewise scale with L –implying an optically thin regime. Therefore, the current data is insufficient to determine the overall optical depth of the absorbing medium.

Investigating the scaling at sample level we find that LRDs (both those in our JWST sample and local ones from Lin et al. 2026) and FeLoBALs span the same relation between L_{bol} and outflow energy (Figure 12) with the only outliers being the $\Delta v = 0$ absorbers from D'Eugenio et al. (2026) and D'Eugenio et al. (2025). The best-fit linear relation shows a slope $m = 0.98 \pm 0.12$ – consistent with the expectations from Equation 18 although the scatter is large, with $\sigma_K = 0.70 \pm 0.1$ dex. This large scatter is likely driven by a combination of projection effects on Δv, imperfect correspondence between $N_H(n = 2)$ and N_H and variation in spatial scales.

If projection effects are a driving factor in the scatter, it may appear that defining $v \equiv |\Delta v| + \sigma$, with σ representing the velocity dispersion of the absorption profile, should reduce the scatter. However, this may not necessarily be the case as σ could be driven by intrinsic turbulent motion. Indeed, as shown in Figure 7, the $v_{turb.}$ values inferred for our sample sources are similar in magnitude to the observed σ. In addition, as discussed in Section 3, σ in Equation 2 is degenerate with τ_0 and hence is poorly recovered by our fitting. Nevertheless, we repeat the earlier analysis using $v \equiv |\Delta v| + \sigma$ as the outflow velocity and find that the slope decreases slightly to $m = 0.82 \pm 0.11$ (Figure 13). While this is still consistent with unity within 2σ, this may indicate gas temperature effects contributing to the σ value once bulk velocities become comparable to v_{turb}. Alternatively, as expected, outflow radius (R) may be decreasing for lower luminosity

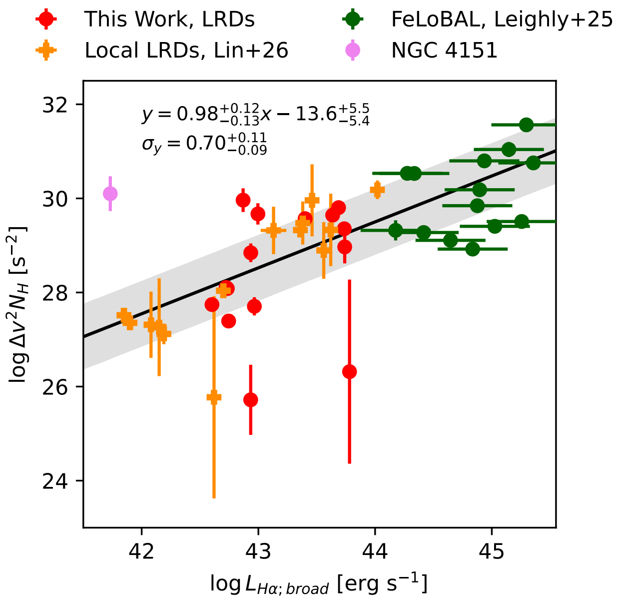

Figure 12. Plot of our sample LRDs (red), Leighly et al. (2025) FeLoBALs (green) and local LRDs from Lin et al. (2026) and Ji in prep. (orange) on the $L_{H\alpha}$ – outflow energy plane. The black line shows the best fit linear regression which shows a slope consistent with 1 as expected from Equation 18. The 0.7 dex scatter is illustrated in gray. The violet point shows NGC 4151 (Hutchings et al. 2002) with the error bar denoting the range of absorber velocity variation. NGC 4151 is a significant outlier with respect to the the LRD – FeLoBAL relation.

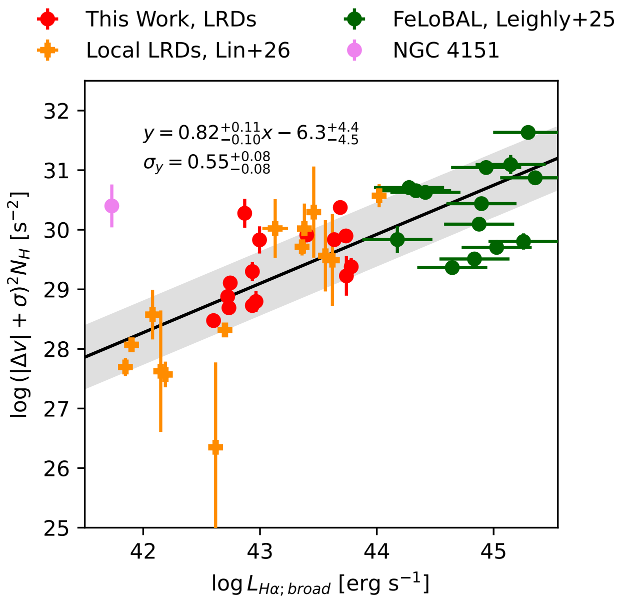

Figure 13. Same as Figure 12 except with $v \equiv |\Delta v| + \sigma$. As can be seen here, the outlier fraction is considerably lower, corresponding to a lower scatter on the inferred relation. The slope remains consistent with 1, however, the slight flattening may be attributed to temperature effects or fit systematics of the σ measurements. As in Figure 12, NGC 4151 (violet) remains an outlying point, possibly due to smaller size of its outflowing region.

AGN, causing their tail to move up on the $v^2 N_H$ axis as R is currently unaccounted for by our measurements. On the other hand, purely instrumental effects, while likely present, can be discounted as the driving force behind the flattening as defining $v \equiv \sigma$ still yields a significant linear relation with $L_{\mathrm{H}\alpha;\mathrm{broad}}$ (Figure 14). However, the slope on the $N_H\sigma^2$–$L_{\mathrm{H}\alpha;\mathrm{broad}}$ $0.53^{+0.12}_{-0.11}$ is significantly flatter than in Figure 12 and Figure 13 suggesting a weaker correspondence between AGN luminosity and Doppler broadening of the absorber. It is currently unclear whether this is driven by physical or instrumental effects.

Assuming that the flattening of the slope in Figure 13 is entirely due to a secondary relation between R and L, we infer $\alpha = 0.26 \pm 0.16$ for this putative relation. This is consistent with slopes of 0.22–0.29 inferred for ionized QSO outflows by Kim et al. (2023). However, the large uncertainties on our estimate mean that a BLR-like $R - L$ relation with $\alpha = 0.5$ cannot be ruled out. Interestingly, the local Seyfert 1 AGN, NGC 4151, appears as a significant outlier in both figures, lying ~ 3 dex above the LRD – FeLoBAL relation. The most likely explanation for this, given the current data, is that the absorbing region in NGC 4151 is considerably smaller than that of LRDs and FeLoBALs, resulting in a higher than expected value of $v^2 N_H$ if R is not taken into account. This is tentatively supported by the rapid variability of the NGC 4151 absorber over 3 month time scales found by Hutchings et al. (2002), who also estimate the absorber to be located at 0.001 pc from the nucleus; ie >3 dex smaller than LRDs and FeLoBALs. However, as LRDs currently lack comparable monitoring of their absorption features, strong conclusions can not be drawn.

The $0.55^{+0.08}_{-0.08}$ dex scatter on the relation in Figure 13 is considerably lower than the 0.7 dex inferred in Figure 12. Assuming that the

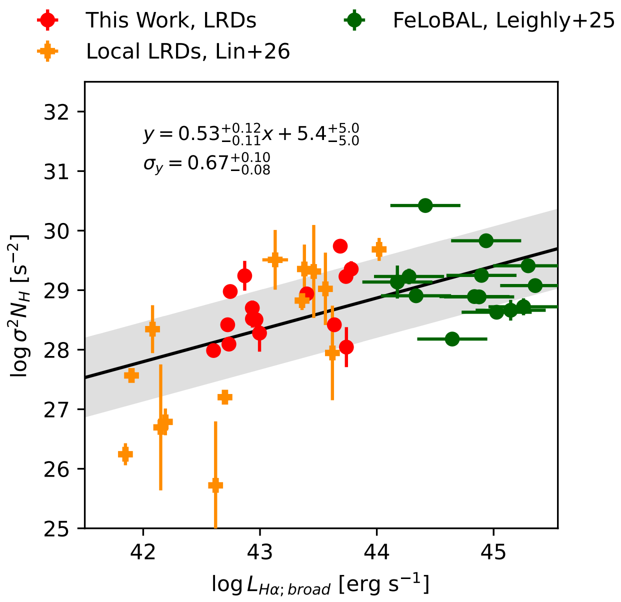

Figure 14. Same as Figure 12 except with $v \equiv \sigma$. As shown here, the correlation remains, however, the slope of 0.53 is considerably flatter than Figure 12, indicating secondary effects driving the broadening of the absorption features.

earlier scatter originates from projection effects and other sources added in quadrature, we obtain $\sigma_{proj.} = 0.43 \pm 0.06$ dex. Considering that projection angle i is expected to be uniformly random on a sample level and assuming a conical outflow geometry, we can attempt to infer the opening angle of this cone through the relation:

$$\Delta v = \Delta v_{int} \sin\left(i + \frac{\theta}{2}\right) \tag{19}$$

where Δv is the observed absorber velocity offset as defined by Equation 2 while Δv_{int} is the intrinsic, deprojected one. Uniformly sampling $i \in [0, 90°]$ we can iteratively solve the above equation for θ, obtaining that $\theta = 54 \pm 9°$ would give the required scatter. This is consistent with the opening angles of the dusty torus inferred for classical AGN, which range from 20° to 60° (Arshakian 2005). This may indirectly point to a scenario in which the poles of the torus in LRDs are occupied by a dense reservoir of gas rather than the more tenuous medium found in the general AGN population. Alternatively, under the assumption that LRDs are LBDs viewed edge-on (Madau & Maiolino 2026a; Geris et al. 2026), our inferred θ is then the angle covered by the torus itself. However, considering the simplicity of the model discussed here, detailed interpretation is premature.

Regardless of the exact interpretation, LRD and FeLoBAL absorbers following the same luminosity scaling suggests that absorption in both is produced by radiative pressure driven outflows. In this scenario, LRD absorbers appear more common than their more luminous counterparts due to lower luminosities of their central engines struggling to drive the dense outflows out into the ISM, causing them to 'loiter' around the nucleus and build up higher column densities. However, a more in-depth comparison across larger samples of both LRDs and FeLoBALs is required to further test this scenario. In particular, extensive R2700 observations are required to decouple τ from σ of the absorption features and accurately capture the outflow energetics in LRDs.

5.3 Parallels with emission line stars - the case for radiatively driven outflows

AGN are not the only systems displaying outflowing Hα absorption. Indeed, luminous blue variable (LBV) stars were among the first systems in which such absorption has been seen (Leitherer & Zickgraf 1987). In LBV systems, the absorption is generated by dense shells of gas ejected during eruption events by radiation-driven winds (van Genderen 2001) and residing at ~ 10 AU scales (Balan et al. 2010). Considering that P Cygni profiles were successfully used in modeling the Hα profiles of LRDs (Matthee et al. 2026; Rusakov et al. 2025) and LRD physics have increasingly been linked with stellar processes (Naidu et al. 2025; de Graaff et al. 2025b; Liu et al. 2026; Naidu et al. 2026), we further compare the energies of LRD and FeLoBAL outflows and winds of LBV stars.

Assembling a reasonable comparison sample of LBVs is not a straightforward task as these systems are known to strongly vary on timescales of months and years owing to their small sizes and unstable nature (Kalari et al. 2018). In addition, some of the parameters of the stellar wind models used to fit P Cygni profiles do not have clear correspondence with parameters of Equation 18. Hence, we utilize the measured velocities of the P Cygni absorption minima as the v parameter and construct our comparison sample from the time averaged Δv and $L_{H\alpha}$ values of P Cygni, η Car and NGC 2363-V1 (Richardson et al. 2010, 2011; Drissen et al. 2001) as well as four additional extragalactic LBVs reported by Guseva et al. (2022, 2024).

The comparison of the LBV stars, our LRDs and Leighly et al. (2025) FeLoBALs is presented in Figure 15 and shows that AGN and LBVs are consistent with the $L \propto \Delta v^2$ relation expected by the simplified model of Equation 18, yet LBVs are offset from the LRD – FeLoBAL sequence by approximately 5 dex with the local Seyfert 1 AGN, NGC 4151, located in between. This is most readily explained by a difference in spatial scales across these systems – the LBV shells have been resolved to be extended on ~10 AU scales (Balan et al. 2010) and the current estimates for NGC 4151 place its absorber at 200 AU from its center (Hutchings et al. 2002). On the other hand, LRD and FeLoBAL absorbers are expected to lie at 1-2 pc or even greater distances from the central engine (Juodžbalis et al. 2024a; Sharma et al. 2025). Following Equation 18, these factors of 10^5–10^3 difference in spatial scales, caused by different lifetimes of AGN episodes and LBV star eruptions, would naturally account for the offset seen on the $L_{H\alpha} - \Delta v^2$ plane. On the other hand, a similarly extreme variation in N_H is unlikely, given that both AGN and stars show similar Hα optical depths and hence likely have similar $N_H(n = 2)$ values.

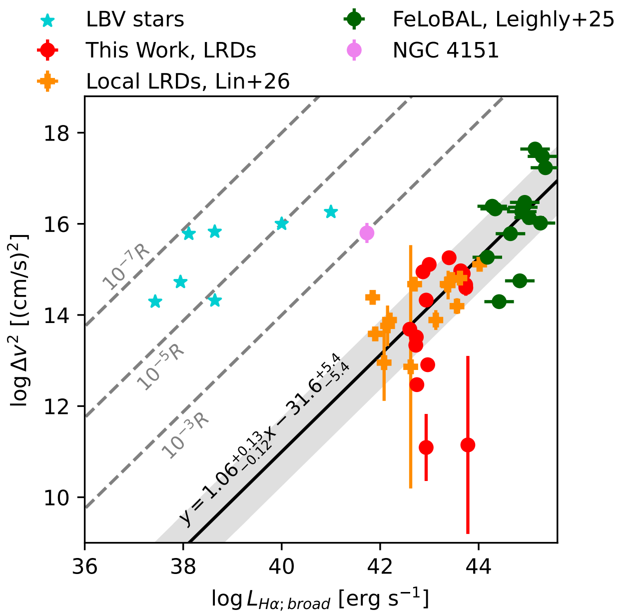

Figure 15. Comparison of the absorber velocity – broad Hα luminosity for our LRDs (red points), local LRDs (orange pluses), FeLoBALs (green points), NGC 4151 (violet point) and LBV stars (blue stars). The solid black line shows the best-fit relation for the AGN sequence with grey shading illustrating the $0.75^{+0.12}_{-0.09}$ dex scatter. The dashed gray lines illustrate the same relation shifted by different physical scales relative to the R for LRDs and FeLoBALs.

The above analysis, however, is still preliminary as our LBV comparison sample is not homogeneous. In addition, at least some LBV eruptions are likely catalyzed by the presence of a companion (Mehner et al. 2010, 2021). Therefore, at least a fraction of the energy in the outflowing shell of some LBVs may be injected from tidal interaction with a companion rather than purely radiatively. The correspondence between these sources breaks down further when considering that the continuum emission of LBVs, by definition, is extremely blue, while LRDs are optically red. Thus, while there are hints that LBV outflows and AGN outflows may be launched through a similar physical mechanism – radiation pressure from a point-like luminous source, a more comprehensive comparison study is needed to conclusively verify the connection between the physics of AGN and stellar absorbers.

Factor	LRDs	FeLoBALs
FeII	Forbidden [Fe II] in the optical, permitted in UV	Ubiquitous permitted FeII emission and absorption
$\langle L_{\rm bol.} \rangle$ [erg s^{-1}]	$10^{45.2}$	$10^{46.9}$
$\langle N_H(n=2) \rangle$ [cm^{-2}]	$10^{14.7}$	$10^{13.9}$
$\langle \lvert \Delta v_{H\alpha} \rvert \rangle$ [km s^{-1}]	164	1975
$\langle L_{bol}/L_{2-10keV} \rangle$	$> 10^4$	1700

Table 3. Summary of the comparisons and mean properties of LRDs and FeLoBALs from Leighly et al. (2025) discussed in the text.

6 CONCLUSIONS

In conclusion, the search for Balmer absorbers in JWST AGN is affected by significant incompleteness, particularly for absorption features observed at rest-frame ($\Delta v = 0$), due to narrow line infill. However, the current data sets are sufficient to show that strong Hα absorbers are a feature of LRDs rather than LBDs with LRDs approaching incidence rates of 40 – 70%, while we constrain an upper limit of 25% incidence of Hα absorption in LBDs. While this is consistent with LRDs showing Balmer breaks in their continua (Setton et al. 2025; Naidu et al. 2025), which are absent in LBDs (Brazzini et al. 2026), both types of faint AGN are similarly X-ray weak (Maiolino et al. 2025; Brazzini et al. 2026; Geris et al. 2026). This suggests that there may be more to the X-ray weakness of faint high redshift JWST AGN than simple obscuration by high hydrogen column densities. While recent theoretical efforts by Sneppen et al. (2026) have shown that apparently unabsorbed broad line profiles can be produced by electron scattering in a high column density environment, we find, consistently with Scholtz et al. (2026b), that exponential broad line profiles are not universally preferred for our sample sources while electron scattering is not the unique interpretation of their shapes (Scholtz et al. 2026b; Madau & Maiolino 2026a,b). Hence, it appears that scenarios invoking radiatively inefficient super-Eddington accretion (Madau & Haardt 2024; Madau 2026) or a missing/weak hot corona (Maiolino et al. 2025) in combination with absorption are the more likely explanations for the near universal X-ray weakness of high redshift AGN.

We also find that the current JWST spectroscopic data sets, which are mostly comprised of R1000 observations, are strongly resolution limited when it comes to accurately assessing the finer properties of Hβ and Hα absorbers found in LRDs with only velocity offsets and equivalent widths reliably recoverable. The higher resolution R2700 gratings mitigate this issue, yet still struggle with recovering weaker rest-frame absorbers with narrow Hα superimposed. This implies that the possibility of all LRDs having Hα absorption can not be discounted by the current data. However, R2700 performs substantially better than R1000 in terms of disentangling Doppler broadening from the effects of optical depth and covering fraction. Hence, large samples of LRDs with R2700 data capturing absorption in multiple hydrogen transitions are required to fully disentangle the $\tau - \sigma - C_f$ degeneracy and constrain the effects of partial covering and emission line infill on the absorber properties. Additionally, in light of the discovery of multiple LRDs at $z < 0.3$ (Ji et al. 2025b; Lin et al. 2025), ground based high resolution ($R \sim 10000$) follow up of these sources offers another highly promising avenue of constraining the physics of the absorbing medium.

In light of the above findings, the statistical power of our sample is rather limited in terms of in-depth constraints on the absorber properties. However, we find that EW$_0$ and Δv are reasonably well recovered in the current data, with similar performance between R1000 and R2700 data. The demographics of our sample across these two parameters reveal that, while absorption is predominantly within $|\Delta v| < 100$ km s^{-1}, once the incompleteness is accounted for, the absorber distribution is skewed towards blueshifted outflows of $\Delta v \approx -300$ km s^{-1} with no absorbers at similar 300 km s^{-1} redshifts, Figure 6. This suggests that the absorption does not originate in a quasi static atmosphere as proposed by the BH* model (Naidu et al. 2025; Liu et al. 2026), but instead resembles the 'Loitering outflows' in FeLoBAL QSOs (Leighly et al. 2025). In addition, we find that EW$_0$ of Hα absorption is uncorrelated with Balmer break strength and considerably larger than stellar atmosphere models predict. This implies either different origins of the UV and optical continua or a diversity in the physical conditions and covering fractions of the absorbing medium – in line with the models of Madau & Maiolino (2026a,b).

The small sample size and intrinsic uncertainties in the fitting mean that extensive discussion of correlations of the absorber properties is largely premature at this stage, with sample sizes larger by a factor of 2-3 required to search for robust relations between the observed properties. Nevertheless, we identify a clear, albeit expected, correlation between $\Delta v_{\rm H\alpha}$ and $\Delta v_{\rm H\beta}$ - consistent with Hα and Hβ absorbers tracing the same gas. The significant deviation of the relation between these velocities together with a lack of correlation between EW$_0$ of the two lines indicates that partial covering and stratification of the absorbing medium are at play - consistent with the earlier findings that the sample absorbers span a spectrum of gas conditions and likely represent clumpy and non-uniform media rather than quasi-static shells of gas. Additionally, we identify a significant correlation between $\Delta v_{\rm H\alpha}$ and $L_{\rm [OIII]}$, potentially implying a common mechanism driving narrow line emission and outflow energetics. If confirmed, this would be direct evidence of the radiation from the BLR escaping into the surrounding medium. Yet, we see only a tentative correlation between L_{1350} and $\Delta v_{\rm H\alpha}$ while no relation between $L_{\rm [OIII]}$ and broad Hα luminosity or L_{5100} is seen. Hence, further investigation is needed to test whether the observed $\Delta v_{\rm H\alpha} - L_{\rm [OIII]}$ correlation is robust. In addition, we do not confirm the correlations claimed in the literature (e.g. Matthee et al. 2026) further highlighting the tentative nature of current statistical analyses.

In terms of absorber energetics, LRDs appear to closely resemble lower luminosity counterparts of FeLoBAL QSOs, occupying the low luminosity – high $N_H(n=2)$ region of the parameter space (Figure 8). The energetics of the absorbing media of both types of sources appear to be consistent with radiation driven outflows (Figure 12). In particular, the relation between Hα luminosities and absorber kinetic energies in LRDs and FeLoBALs mimics that of luminous blue variable (LBV) stars (Figure 15), with the offset accountable for by the currently loosely constrained outflow radii (R). This finding offers a potential avenue towards a unified LRD-QSO framework in which the prevalence and column densities of Balmer absorbers in LRDs can be accounted for through a combination of lower luminosities and lower metallicities producing an abundance of loitering outflows. Such high density, low metallicity environments may also be able to explain the lack of standard FeII emission in LRDs through suppression of the UV and optical FeII emission by Balmer continuum absorption and reduced presence of iron respectively. However, a more careful analysis of the properties of these two AGN populations is needed to fully establish whether a unified framework is at play. In particular, high resolution (R2700) JWST observations of LRDs are required in order to decouple absorber kinematics from radiative transfer effects, while constraints on FeII emission properties in LRDs will generally require deep low and medium resolution spectra.

Lastly, the parallels between nuclear AGN outflows and those driven by LBV stars offer an intriguing window into how radiatively driven outflows operate across different spatial scales. However, the current comparisons are limited as only v and $N_{\rm H}(n = 2)$ can be constrained by the current data. Therefore, observations of local LRDs, luminous FeLoBALs and LBV stars with state of the art optical interferometers, like GRAVITY+ (GRAVITY+ Collaboration et al. 2022, 2026), aimed at resolving the Hα absorbers are needed to establish whether AGN and stellar outflows truly share the same scaling relation.

ACKNOWLEDGEMENTS

IJ acknowledges support by the Huo Family Foundation through a P.C. Ho PhD Studentship. XJ, FDE, JS and RM acknowledge support by the Science and Technology Facilities Council (STFC), by the ERC through Advanced Grant 695671 "QUENCH", and by the UKRI Frontier Research grant RISEandFALL. RM also acknowledges funding from a research professorship from the Royal Society. EB acknowledges funding from the Bando Ricerca Fondamentale INAF 2024 (GO grant "A JWST/MIRI MIRACLE: Mid-IR Activity of Circumnuclear Line Emission" and MiniGrant RSN1 1.05.24.07.01). AJB acknowledges funding from the "FirstGalaxies" Advanced Grant from the European Research Council (ERC) under the European Union's Horizon 2020 research and innovation programme (Grant agreement No. 789056). SC and GV acknowledge support by European Union's HE ERC Starting Grant No. 101040227 - WINGS. GC acknowledges support from the INAF GO grant 2024 "A JWST/MIRI MIRACLE: MidIR Activity of Circumnuclear Line Emission". ECL acknowledges support of an STFC Webb Fellowship (ST/W001438/1). BER, ZM and JZ acknowledge support from the NIRCam Science Team contract to the University of Arizona, NAS5-02105, and JWST Program 3215. HÜ acknowledges support by the Max Planck Society through the Lise Meitner Excellence Program. HÜ acknowledges funding by the European Union (ERC APEX, 101164796). Views and opinions expressed are however those of the authors only and do not necessarily reflect those of the European Union or the European Research Council Executive Agency. Neither the European Union nor the granting authority can be held responsible for them. GV acknowledges financial support from the Italian National Institute for Astrophysics (INAF) under the IAF - Astrophysics Fellowships in Italy grant CUP C59J21034720001 (AD MAJORA).

DATA AVAILABILITY

All data used in this study is publicly available as part of JADES DR4 (Curtis-Lake et al. 2026) as well as in MAST `https://mast.stsci.edu/portal/Mashup/Clients/Mast/Portal.html` and the Dawn JWST archive – `https://dawn-cph.github.io/dja/`.

REFERENCES

Ananna T. T., Bogdán Á., Kovács O. E., Natarajan P., Hickox R. C., 2024, ApJ, 969, L18
Anderson K. S., Kraft R. P., 1969, ApJ, 158, 859
Aoki K., Iwata I., Ohta K., Ando M., Akiyama M., Tamura N., 2006, ApJ, 651, 84
Arshakian T. G., 2005, A&A, 436, 817
Asada Y., Inayoshi K., Fei Q., Fujimoto S., Willott C., 2026, arXiv e-prints, p. arXiv:2601.10573
Balan A., Tycner C., Zavala R. T., Benson J. A., Hutter D. J., Templeton M., 2010, AJ, 139, 2269
Bennert N., Jungwiert B., Komossa S., Haas M., Chini R., 2006, A&A, 456, 953
Bischetti M., et al., 2023, ApJ, 952, 44
Blustin A. J., Page M. J., Fuerst S. V., Branduardi-Raymont G., Ashton C. E., 2005, A&A, 431, 111
Brazzini M., D'Eugenio F., Maiolino R., Juodžbalis I., Ji X., Scholtz J., Chang S.-J., 2025, MNRAS, 544, L167
Brazzini M., et al., 2026, arXiv e-prints, p. arXiv:2601.22214
Bunker A. J., et al., 2023, arXiv e-prints, p. arXiv:2306.02467
Casey C. M., Akins H. B., Kokorev V., McKinney J., Cooper O. R., Long A. S., Franco M., Manning S. M., 2024, ApJ, 975, L4
Choi H., Leighly K. M., Terndrup D. M., Dabbieri C., Gallagher S. C., Richards G. T., 2022, ApJ, 937, 74
Comastri A., et al., 2026, A&A, 706, A302
Curtis-Lake E., et al., 2026, MNRAS, 549, stag836
D'Eugenio F., et al., 2024, arXiv e-prints, p. arXiv:2404.06531
D'Eugenio F., et al., 2025, arXiv e-prints, p. arXiv:2510.00101
D'Eugenio F., et al., 2026, MNRAS, 545, staf2117
Drissen L., Crowther P. A., Smith L. J., Robert C., Roy J.-R., Hillier D. J., 2001, ApJ, 546, 484
Eisenstein D. J., et al., 2023, arXiv e-prints, p. arXiv:2306.02465
Elvis M., 2000, ApJ, 545, 63
Escott E. L., et al., 2025, MNRAS, 536, 1166
Finkelstein S. L., et al., 2023, ApJ, 946, L13
Foreman-Mackey D., Hogg D. W., Lang D., Goodman J., 2013, PASP, 125, 306
Furtak L. J., et al., 2024, Nature, 628, 57
GRAVITY+ Collaboration et al., 2022, A&A, 665, A75
GRAVITY+ Collaboration et al., 2026, A&A, 707, A115
Geris S., et al., 2026, arXiv e-prints, p. arXiv:2606.21614
Greene J. E., et al., 2026, ApJ, 996, 129
Guseva N. G., Thuan T. X., Izotov Y. I., 2022, MNRAS, 512, 4298
Guseva N. G., Thuan T. X., Izotov Y. I., 2024, MNRAS, 527, 3932
Hainline K. N., et al., 2025, ApJ, 979, 138
Harikane Y., et al., 2023, ApJ, 959, 39
Hutchings J. B., Crenshaw D. M., Kraemer S. B., Gabel J. R., Kaiser M. E., Weistrop D., Gull T. R., 2002, AJ, 124, 2543
Hviding R. E., et al., 2025, A&A, 702, A57
Hviding R. E., et al., 2026, ApJ, 1000, L18
Inayoshi K., Maiolino R., 2024, arXiv e-prints, p. arXiv:2409.07805
Ishikawa Y., et al., 2026, arXiv e-prints, p. arXiv:2607.09647
Ivey L. R., et al., 2026, MNRAS,
Ji X., et al., 2025a, arXiv e-prints, p. arXiv:2501.13082
Ji X., et al., 2025b, arXiv e-prints, p. arXiv:2507.23774
Ji X., et al., 2026, arXiv e-prints, p. arXiv:2604.03370
Juodžbalis I., et al., 2024a, MNRAS, 535, 853
Juodžbalis I., et al., 2024b, Nature, 636, 594
Juodžbalis I., et al., 2026a, MNRAS, 546, stag086
Juodžbalis I., et al., 2026b, Nature, 653, 1017
Kalari V. M., Vink J. S., Dufton P. L., Fraser M., 2018, A&A, 618, A17
Kim C., Woo J.-H., Luo R., Chung A., Baek J., Le H. A. N., Son D., 2023, ApJ, 958, 145
Knop R. A., Armus L., Larkin J. E., Mathews K., Shupe D. L., Soifer B. T., 1996, AJ, 112, 81
Kocevski D. D., et al., 2023, ApJ, 954, L4
Labbé I., et al., 2024, arXiv e-prints, p. arXiv:2412.04557

Laor A., 2006, ApJ, 643, 112
Leighly K. M., Terndrup D. M., Lucy A. B., Choi H., Gallagher S. C., Richards G. T., Dietrich M., Raney C., 2019, ApJ, 879, 27
Leighly K. M., Gallagher S. C., Choi H., Terndrup D. M., Voelker J. R., Richards G. T., Morabito L. K., 2025, ApJ, 993, 129
Leitherer C., Zickgraf F.-J., 1987, A&A, 174, 103
Li J., et al., 2017, ApJ, 846, 79
Lin X., et al., 2025, arXiv e-prints, p. arXiv:2507.10659
Lin X., et al., 2026, arXiv e-prints, p. arXiv:2605.21574
Liu H., Luo B., Brandt W. N., Gallagher S. C., Garmire G. P., 2018, ApJ, 859, 113
Liu H., Jiang Y.-F., Quataert E., Greene J. E., Ma Y., Lin X., 2026, arXiv e-prints, p. arXiv:2603.02317
Madau P., 2026, A&A, 708, A116
Madau P., Haardt F., 2024, ApJ, 976, L24
Madau P., Maiolino R., 2026a, arXiv e-prints, p. arXiv:2602.22386
Madau P., Maiolino R., 2026b, arXiv e-prints, p. arXiv:2605.05074
Madau P., Maiolino R., Scholtz J., D'Eugenio F., 2026, arXiv e-prints, p. arXiv:2604.04216
Maiolino R., et al., 2024a, Nature, 627, 59
Maiolino R., et al., 2024b, A&A, 691, A145
Maiolino R., et al., 2025, MNRAS, 538, 1921
Maiolino R., et al., 2026, MNRAS, 548, staf2109
Marconi A., Axon D. J., Maiolino R., Nagao T., Pastorini G., Pietrini P., Robinson A., Torricelli G., 2008, ApJ, 678, 693
Matthee J., et al., 2024, ApJ, 963, 129
Matthee J., et al., 2026, arXiv e-prints, p. arXiv:2603.17667
Mehner A., Davidson K., Ferland G. J., Humphreys R. M., 2010, ApJ, 710, 729
Mehner A., et al., 2021, A&A, 655, A33
Morabito L. K., Dai X., Leighly K. M., Sivakoff G. R., Shankar F., 2011, ApJ, 737, 46
Naidu R. P., et al., 2025, arXiv e-prints, p. arXiv:2503.16596
Naidu R. P., et al., 2026, arXiv e-prints, p. arXiv:2606.30711
Netzer H., Wills B. J., 1983, ApJ, 275, 445
Oke J. B., Gunn J. E., 1983, ApJ, 266, 713
Pérez-González P. G., et al., 2026, arXiv e-prints, p. arXiv:2602.20247
Planck Collaboration et al., 2020, A&A, 641, A6
Rakić N., 2022, MNRAS, 516, 1624
Richardson N. D., Gies D. R., Henry T. J., Fernández-Lajús E., Okazaki A. T., 2010, AJ, 139, 1534
Richardson N. D., Morrison N. D., Gies D. R., Markova N., Hesselbach E. N., Percy J. R., 2011, AJ, 141, 120
Rinaldi P., et al., 2026, arXiv e-prints, p. arXiv:2604.07138
Rogerson J. A., Hall P. B., Snedden S. A., Brotherton M. S., Anderson S. F., 2011, New Astron., 16, 128
Rusakov V., et al., 2025, arXiv e-prints, p. arXiv:2503.16595
Sacchi A., Bogdán Á., 2025, ApJ, 989, L30
Savage B. D., Sembach K. R., 1991, ApJ, 379, 245
Scholtz J., et al., 2026a, MNRAS,
Scholtz J., et al., 2026b, arXiv e-prints, p. arXiv:2603.22277
Setton D. J., et al., 2025, ApJ, 995, 118
Sharma M., Arav N., Korista K. T., Bautista M., Dehghanian M., Byun D., Walker G., Mintz S., 2025, A&A, 693, A254
Sneppen A., et al., 2026, arXiv e-prints, p. arXiv:2601.18864
Sok V., et al., 2026, arXiv e-prints, p. arXiv:2606.23778
Stern J., Laor A., 2012, MNRAS, 423, 600
Sun W. Q., et al., 2026, arXiv e-prints, p. arXiv:2601.20929
Tang M., et al., 2026, arXiv e-prints, p. arXiv:2604.03563
Trefoloni B., et al., 2025, A&A, 700, A203
Vito F., Brandt W. N., Luo B., Shemmer O., Vignali C., Gilli R., 2018, MNRAS, 479, 5335
Wang B., et al., 2024, arXiv e-prints, p. arXiv:2403.02304
Wills B. J., Netzer H., Wills D., 1985, ApJ, 288, 94
Yue M., Eilers A.-C., Ananna T. T., Panagiotou C., Kara E., Miyaji T., 2024, ApJ, 974, L26
Zanchettin M. V., et al., 2023, A&A, 679, A88
de Graaff A., et al., 2025a, A&A, 697, A189
de Graaff A., et al., 2025b, A&A, 701, A168
van Genderen A. M., 2001, A&A, 366, 508

APPENDIX A: Hα ABSORPTION FITS

Here we show the Hα profile fits to sources not displayed in Figure 2.

APPENDIX B: Hβ ABSORPTION FITS

Here we show the combined Hβ and [O III] doublet fits for the sample sources with Hβ absorption.

This paper has been typeset from a TEX/LATEX file prepared by the author.

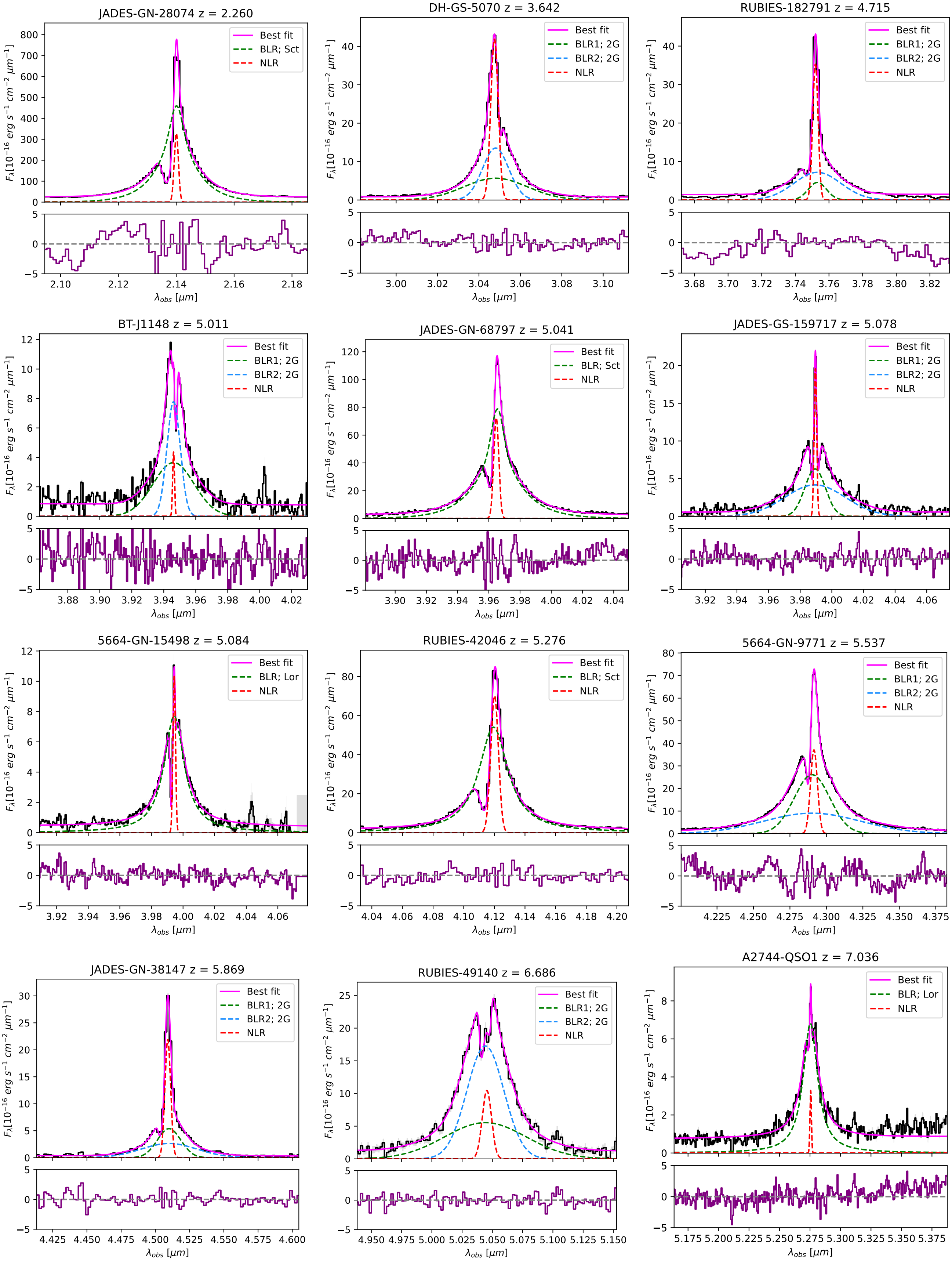

Figure A1. Showcase of the fits to the sample sources not shown in Figure 2. The notation is the same as in the latter figure.

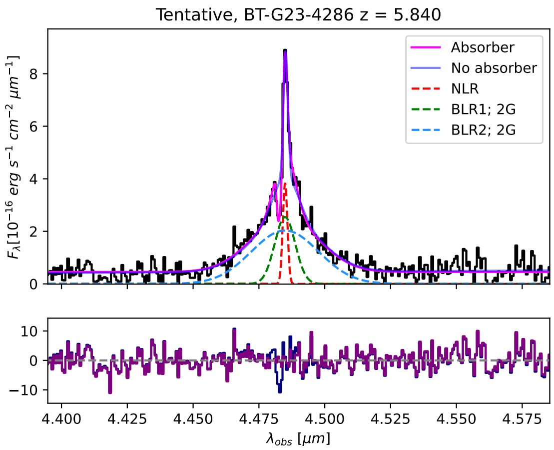

Figure A2. Broad Hα profile of BT-G23-4286, the tentative absorber found in our sample. The lines have the same meaning as in Figure A1 except the translucent blue line shows the fit without an absorbtion feature with the corresponding residuals shown in dark blue in the panel below. While the no absorber fit residual appears significant, the overall scale of the residuals is a factor of 2 larger than in Figure A1, due to underestimation of errors by the IFU pipeline.

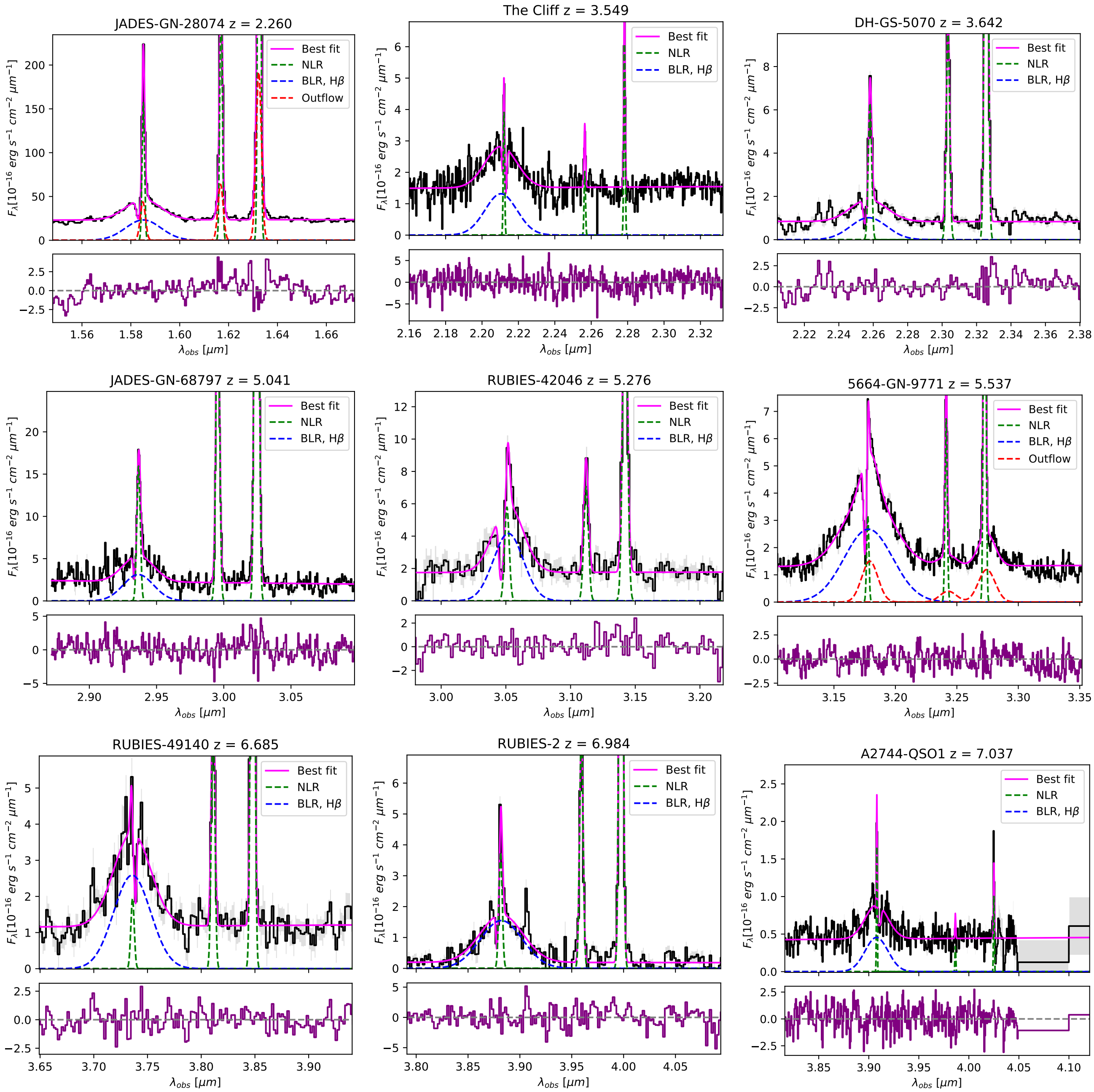

Figure B1. Showcase of the fits to the broad Hβ and [O III] doublet of the sample sources with Hβ absorption. The combined fit is shown in magenta, the broad Hβ – in blue, the narrow lines are plotted in green, while outflows, if present, are plotted in red.